Efficient computational mesoscale modeling of concrete under cyclic loading

Thomas Titscher

Thesis by compendium of publications

Efficient computational mesoscale modeling of concrete under cyclic loading

DEPARTAMENT D'ENGINYERIA CIVIL I AMBIENTAL (DECA)

PROGRAMA DE DOCTORAT EN ANÀLISI ESTRUCTURAL

July 5, 2019

PhD Student	Dipl.-Ing. Thomas Titscher
Thesis supervisor	Professor Xavier Oliver
	Universitat Politècnica de Catalunya (UPC/BarcelonaTech)
	Barcelona, Spain
Second supervisor	Dr. Jörg F. Unger
	Federal Institute for Materials Research and Testing (BAM)
	Berlin, Germany

Abstract

Concrete is a complex material and can be modeled on various spatial and temporal scales. While simulations on coarse scales are practical for engineering applications, a deeper understanding of the material is gained on finer scales. This is at the cost of an increased numerical effort that can be reduced by the three methods developed and used in this work, each corresponding to one publication.

The coarse spatial scale is related to fully homogenized models. The material is described in a phenomenological approach and the numerous parameters sometimes lack a physical meaning. Resolving the three-phase mesoscopic structure consisting of aggregates, the mortar matrix and the interfaces between them allow to describe similar effects with simpler models. This work addresses two computational challenges related to mesoscale modeling.

First, aggregate particles take up a high volume fraction and an efficient particle-packing algorithm is required to generate non-overlapping, random mesostructures. Enforcing an additional distance between the aggregates is essential to obtain undistorted meshes for finite element simulations, but further complicates the packing problem. An event-driven molecular-dynamics algorithm is applied to this problem that, in contrast to traditional methods, allows movement and a dense arrangement of the aggregates. This allows creating concrete mesostructures with realistic aggregate volume fractions.

The second challenge concerns stability problems in mesoscale simulations of concrete fracture. The geometric complexity and the combination of three material laws for each of the phases leads to numerical instabilities, even for regularized material models. This requires tiny time steps and numerous iterations per time step when integrated with a classic backward Euler scheme. The implicit–explicit (IMPL-EX) integration extrapolates internal variables that account for the nonlinear behavior. This linearizes the equations, provides additional robustness and a computational speedup. In combination with a novel time step control method, a three-dimensional mesoscale compression test is accelerated by a factor of 40, compared to an adaptive backward Euler algorithm.

The life time of concrete under cyclic loads is commonly predicted with empirical Wöhler lines. They relate the number of endured cycles with the applied load amplitude and can be included in constitutive formulations. They can, however, hardly be generalized to geometries and load configurations other than the ones tested.

On a finer temporal scale, fatigue failure is modeled by the accumulation of damage

within each loading cycle. This resolves the whole process of failure, includes stress redistributions and size effects and can easily be extended to multiphysics phenomena.

The third computational challenge solved here is the efficient temporal integration that would not be feasible in a naive cycle-by-cycle integration of thousands or millions of cycles. The cost of evaluating a single cycle is reduced by reformulating the problem in the frequency space. It is sufficient to equilibrate the structure once for each Fourier coefficient which significantly speeds up this evaluation. The accumulated damage of one cycle is integrated in time using an adaptive cycle jump concept. For a two dimensional void test structure, the combination of both techniques leads to a 25 times faster simulation compared to the full integration.

These three main contributions decrease the numerical cost of mesoscale simulations, allow larger and more detailed models and are a basis to deepen the understanding of the complex failure patterns in concrete.

Thomas Titscher

Contents

Contents

1 Motivation

1.1 Introduction

Concrete is one of the most attractive building materials consumed by humans more than any other material, except water. 5% of worldwide CO2 emissions are created from the cement industry. The conservation of natural resources is a key challenge for the next decades. This can be achieved by increasing the lifetime of concrete structures with a robust, lifetime oriented design. For this purpose, a reliable numerical model to predict the performance of concrete over its lifetime is required. The investigation of the fatigue behavior of concrete has been an ongoing research topic for many decades. However, neither experiments nor theoretical works nor numerical simulations could fully explain the complex processes that lead to fatigue failure.

Lifetime aspects including fatigue failure of concrete structures were traditionally only of minor importance due to the limited amplitude of the applied cyclic loads compared to the constant dead load. Because of the growing interest in maxing out the capacities of concrete, its fatigue failure under compression has become an important issue. Typical examples are offshore wind energy plants, which undergo extreme loading conditions of non-uniform amplitudes arising from wind and waves or fatigue loading of bridges with a steady increase of traffic weight. However, a variety of interacting phenomena such as e.g. loss of prestress, degradation due to chemical reactions or creep and shrinkage influence the fatigue resistance. As a consequence, it is difficult to estimate the lifetime using only experimental techniques. Furthermore, failure due to cyclic loads is generally not instantaneous, but characterized by a steady damage accumulation. Therefore, a reliable numerical model to predict the performance of concrete over its lifetime is required, which accurately captures order effects and full three-dimensional stress states.

Applications of such simulations are diverse. In the dimensioning of an engineering structure, more precise models can reduce uncertainties and the possibly redundant material associated with it. In the fundamental research of material models, the importance of several physical aspects in a material theory can be evaluated by adding or removing them from a numerical model. This helps to understand to which extend certain phenomena explain a measured material response. And another example is the recently advancing concept of digital twins, where a numeric representation of a specimen is constantly updated with measured data from its real-world counterpart to better predict its behavior.

The challenge of modeling concrete material behavior is its complex internal geometry and its nonlinear constitutive relationship. Its fracture process consists of the formation of a broad distribution of microscopic cracks which coalesce and form a macrocrack. This process is triggered by inhomogenities in the material. Theoretically, one can think of a simulation that covers the whole material life time including the manufacturing process with all the physical details on length scales down to (sub)atom level. Practically, however, suitable compromises have to be found that resolve certain physical or geometrical aspects while approximating the rest.

The simulation of concrete in a fully homogenized manner means smearing of all concrete components to a homogeneous material that reproduces the macroscopic behavior. The model resolution is chosen to represent the structural geometry. This is a rather coarse representation, compared to resolving the complex internal material structure. This resolution correlates with the numerical effort to solve such a model, which leads to the main advantage of these methods: the calculations are very fast. In return, the upper-scale phenomenological modeling of the heterogeneous internal concrete structure leads to very complex constitutive models. That includes numerous parameters that may lack a direct physical interpretation. They are determined by parameter fitting with experimental data and their validity is restricted to certain load cases.

The modeling of concrete on the mesoscale allows the resolution of the internal concrete structure, consisting of aggregates, the mortar matrix and the interfacial transition zone in between. The complex failure processes can then be represented with simpler constitutive models for each of the three components. This, however, comes at the disadvantage of increased computational cost and stability issues of the numeric solution.

In quasistatic material models for concrete, the fracture processes only progress when a new load maximum is reached. Fatigue behavior is modeled with the modification to allow fracture progression on every load change – even well below this historic maximum. This means that every loading cycle has to be resolved and numerical methods that deal with the corresponding computational cost have to be employed. The benefit compared to approaches that only predict the ultimate failure point, is that this models the whole material lifetime. It automatically resolves stress redistributions and can be coupled in a multiphysics context.

1.2 Structure and aim of the work

The goal of this work is to provide a framework of numerical methods that deal with the numerical costs of mesoscale simulations for both quasistatic and cyclic loading. The physical background of concrete modeling is presented first, focusing on the mesoscale geometry, continuum damage mechanics and fatigue models. The resulting numerical issues are shown and solved next.

Thomas Titscher

The complex mesoscale structure consists of a dense aggregate packing. The main challenge is to simulate this packing numerically. Therefore, an event-driven molecular-dynamics algorithm is employed and adapted. Its growing and moving particles create geometries with a realistically high aggregate volume fraction.

Next, this geometry is used in fracture simulations of mesoscale concrete. Softening materials for both the interfacial transition zone and the cement matrix are employed and the arising localization and stability issues are identified. Here, the implicit-explicit (IMPL-EX) integration scheme provides additional robustness that results in a performance benefit compared to backward Euler solution schemes.

Finally, the high numerical cost of fatigue simulations is addressed. In a full time integration of a structure under cyclic loading, each of the possibly millions of loading cycles has to be divided into multiple steps per cycle. This high temporal resolution clearly exceeds the computational resources. Two optimization techniques are combined to reduce both the cost of evaluating a single loading cycle and the overall number of cycle evaluations.

2 Nonlinear physical aspects of concrete modeling

Concrete is a complex material with a heterogeneous geometry and a multitude of physical phenomena. Main ingredients are cement, water and aggregates which are mixed during the manufacturing process. The cement chemically binds the water in an exothermic reaction that builds calcium silicon hydrate (C-S-H) on the nanostructure [Allen et al. 2007; Bullard et al. 2011; Hlobil et al. 2016] and the fluid concrete mixture gradually hardens. The generated heat is released over the materials outer surface which creates a temperature gradient towards the center. This already introduces thermal stresses and even microscopic defects to the material. Concrete reaches the majority of its strength within a few weeks after casting. The chemical reactions, however, go on for years or decades and further stiffen the microstructure.

The hardened cement phase contains a complex pore structure with pore diameters in the range of nano meters up to centimeters [Mindess et al. 2003]. It contains a mixture of air, fluid water and water vapor that is heavily influenced by the temperature and humidity of the surrounding air. Hygroscopic [Bažant et al. 1972; Johannesson et al. 2010] and thermo-hygroscopic [Gawin et al. 2011] models describe the corresponding transport processes and phase transitions. As an example, fire induced spalling is a failure mechanism based on these processes. A high temperature gradient causes the water to evaporate. It is released near the materials surface but causes high pore pressures below the surface where the water transport is hindered.

When concrete is exposed to a rather low mechanical load for a long time, it shows a slow but steady deformation that is commonly modeled with creep models [Bažant et al. 1988]. The hygro-thermal processes caused by the long exposure to the environmental conditions, however, cannot be neglected. Similar considerations are important in long lasting fatigue experiments. This generally complicates the material modeling since a single physical aspect can hardly be isolated in experiments.

On the shorter time scale of fracture experiments, failure occurs within minutes of loading and it is reasonable to focus purely on mechanical models. But these models can indirectly include hygroscopic effects, e.g. in the description of the interfacial transition zone (ITZ). It is a narrow zone (about $20\,\mu m$) surrounding the concrete aggregates. During drying, aggregates absorb water from this zone which leads to a more brittle and less durable microstructure compared to the surrounding cement matrix material [Ollivier

et al. 1995]. This is observable in fracture experiments, where material deterioration and damage starts in the ITZ. It effectively debonds the aggregates and leads to a stress redistribution within the cement matrix. Macroscopic cracks in the cement connect the damaged ITZs and lead to material failure. Resolving these processes with separate material models for the cement matrix, the aggregates and the ITZ is often referred to as mesoscale modeling [Wriggers et al. 2006; Unger et al. 2011b].

Note that the nano and micro structures of the phases are smeared into one model. During this homogenization, some information on the complex material response on lower scales is lost and has to be modeled. But the main failure process – the ITZ deterioration with subsequent cement matrix cracks – can be resolved. Fully homogenized models smear the properties of all phases into a single one. It is quite evident that obtaining a similar material response requires more complex material models with parameters that are no longer associated to the single material phases.

2.1 Mesoscale geometry

The mesoscale of concrete describes a scale that resolves the aggregates by the geometry, usually in the order of millimeters and above. Aggregates are the filler material of a concrete mix and consists of sand, gravel, crushed rock and many other hard materials in various shapes and sizes. Their size distribution heavily influences the mechanical properties of concrete and is the topic of mix design optimization [Hüsken et al. 2008].

For a numerical analysis, the aggregate geometry has to be obtained. One way is the X-ray microtomography. A three dimensional voxel image is reconstructed from multiple scans of a real concrete specimen [Nagai et al. 2006]. Depending on its value, each voxel is assigned to either matrix or aggregate material [Nguyen et al. 2015]. This accurately captures the mesoscale geometry but has some practical drawbacks. The specimen size is limited to the X-ray system and scanning multiple samples to represent the variations in the material is time consuming.

An alternative is a simulated mesoscale geometry that approximates real concrete aggregate mixtures. The latter ones are defined via grading curves or sieve curves [DIN 1045 2008] and describe the aggregate mass distribution. Practically, the aggregate mixture is poured over a sieve with a certain sieve size. The weight of all aggregates that remain in the sieve is measured. This is repeated for several sieve sizes. The result can be interpreted as a cumulative density function (CDF) for the aggregate mass. This concept is illustrated for three example distributions in Fig. 2.1.

The monodisperse distribution in Fig. 2.1a is characterized by a single aggregate diameter d^*. All aggregates are able to pass a sieve with sieve size $> d^*$ and remain in it for a sieve size $< d^*$. Thus, all aggregates have a size d^*. A bidisperse distribution is defined by two diameters and corresponding mass fractions and is shown in Fig. 2.1b. All the

(a) Monodisperse   (b) Bidisperse   (c) Polydisperse
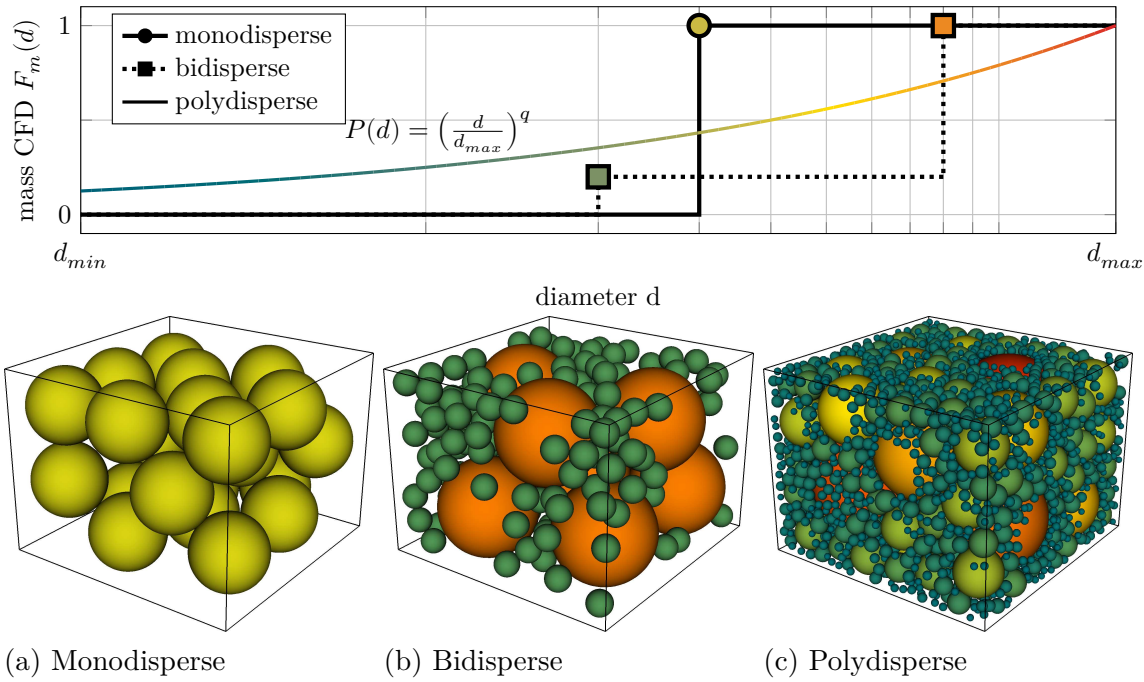
Figure 2.1: Size distributions for the particle diameter d between a minimal $(d_{\min})$ and maximal $(d_{\max})$ diameter.

aggregate mass is above the bigger diameter and only the fraction of smaller aggregates below it.

Real concrete mixtures are described by continuous distributions, similar to the one depicted in Fig. 2.1c. A discrete set of aggregates is picked randomly from this distribution until the required total aggregate mass is obtained. The numerical problem of packing these aggregates into a virtual specimen is further discussed in Section 3.1.

2.2 Fracture modeling

Material fracture or failure occurs if an applied external load exceeds the load carrying capacity of the material. This then leads to an actual separation of parts of the material.

Materials like glass, crystalline materials or a variety of materials at low temperature exhibit brittle failure. With gradually increasing load, the material behaves elastically until it shatters instantaneously [Campbell 2012]. Ductile materials, like metals, on the other hand, exhibit a different failure process. After an initial elastic phase, plastic deformations occur and permanently change the shape of the structure, even after removing the loads. For some technical applications, this point already defines material failure, as the function of the material may be lost. As the load increases further, microscopic
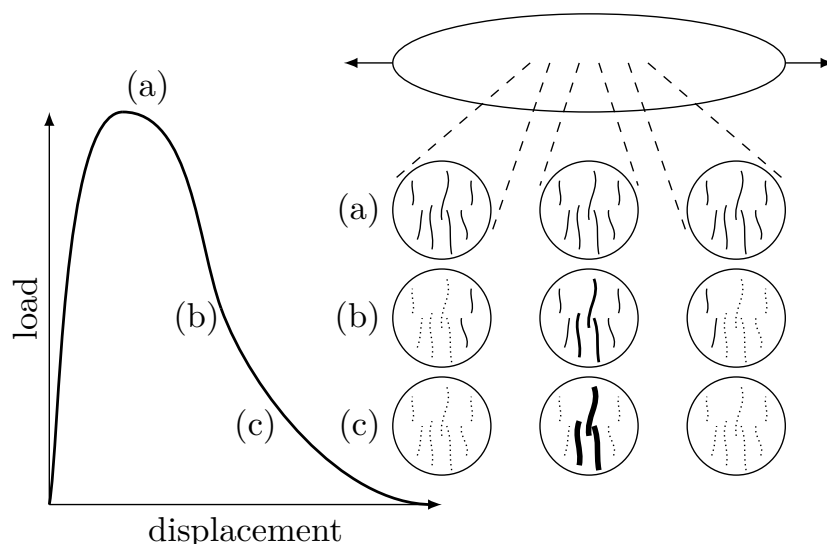
Figure 2.2: Failure pattern of quasi-brittle materials, according to [Poh et al. 2017].

voids form and connect to cracks. These cracks propagate through the material and effectively reduce the load carrying cross chapter of the material. The increased load on the remaining material then causes a spontaneous (brittle) failure.

The behavior of concrete, similar to rocks, some ceramics, or ice, is characterized as quasibrittle. The pre-peak behavior, again, is mostly linear elastic with the initial material stiffness. Towards the peak load, microscopic cracks form in a broad region, see Fig. 2.2a. A further increase of the external displacements now causes strain softening. Defects from the drying or geometric notches (e.g. aggregates) form slightly weaker regions where the microcracks grow faster. This further weakens the regions, their strains increase and the surrounding material unloads. This is depicted in Fig. 2.2b where opening microcracks are illustrated thick and dotted microcracks close. This process continues and forms a band of high strains, the localized zone in Fig. 2.2c.

2.2.1 Constitutive description

A framework for the material description is given by balance equations. Elastic material laws can be derived from the non-dissipative conservation of momentum. Including plastic deformation and damage introduces energy dissipation. Thus, the laws of thermodynamics, or more precisely, the Clausius-Duhem inequality or dissipation inequality have to be fulfilled [Truesdell 1952]. They ensure the irreversibility of natural processes such as the disability for damaged materials to heal.

The constitutive description of a material depends on its geometric representation. In **continuum models**, the governing equations are formulated for a continuous medium in terms of a stress-strain relationship. A simple example is Hooke's law that describes

isotropic linear elastic material. Continuum models will be the focus of this work and are described in the next chapter, but alternatives are briefly discussed here.

Discrete models describe the material as an assembly of elementary entities such as springs, bars, beams, spheres and many more. Associated constitutive models are formulated in terms of forces and relative displacements. Truss or beam structures are simple examples that can be extended to model fracture. *Lattice models* represent the material as a fine grid (lattice) of beam elements that break, if a critical force is reached [Schlangen et al. 1992]. They are also applied to mesoscale simulations. An aggregate structure is projected to the lattice and the beam material properties are assigned accordingly. Beams within an aggregate have a higher stiffness and endure more forces than matrix beams. Beams that cross the aggregate-matrix interface are further weakened to represent the ITZ. A Voronoi triangulation can reduce the directional bias of the regular lattice structure [Cusatis et al. 2011] and more sophisticated force-displacement laws can include damage and plasticity under cyclic loading [Grassl et al. 2008].

The *distinct element method* approximates the body with closely packed particles and imposes force-displacement relationships between them to model the material behavior. These forces hinder particle overlaps and model friction in granular soil simulations [Cundall et al. 1979]. Solid materials are modeled with a stiffer relationship and fracture can be introduced with a sudden drop of transmissible forces after a defined tensile strength [Zubelewicz et al. 1987].

An alternative are continuum models with embedded discontinuities. The idea is to enhance the finite element discretization of a continuum model (often, but not necessarily linear elastic) with a description of a discrete crack or a highly localized zone. This description is provided by *fracture mechanics* that deals with stress singularities at the crack tip and provides criteria for crack initiation and propagation [Erdogan et al. 1963]. The stress-free (Griffith) crack [Griffith 1921] is suitable for brittle materials, but cannot model the softening response in quasibrittle materials. Instead, cohesive cracks are used that relate the transferable traction over a crack with its opening or separation [Hillerborg et al. 1976]. Extended finite elements [Belytschko et al. 1999; Moës et al. 1999; Moës et al. 2002; Unger et al. 2007; Loehnert et al. 2011] excel at modeling a single crack by inserting the traction-separation law within continuous elements. But especially in a three-dimensional setting, this results in a cumbersome geometry problem [Paul et al. 2017]. A less invasive alternative is placing the traction-separation laws on the edges/faces of an existing finite element mesh. Accurately tracking the a priori unknown crack path, however, may require frequent adjustments of the mesh. A computationally expensive resort is to allow discontinuities at every finite element edge [Carol et al. 2001]. A more suitable application arises for known crack paths, mostly at interfaces within the material. Examples are the rebar-concrete interface for reinforced concrete [Lundgren et al. 2000] or the ITZ [Unger et al. 2011b].

Interestingly, traction-separation laws can be regarded as a limit case of continuum damage models [Simo et al. 1993]. In the continuum strong discontinuity approach (CSDA)

very thin continuum damage elements with appropriate stress-strain laws resemble the behavior of traction-separation laws [Oliver et al. 2002]. This allows modeling these interfaces with only continuum damage mechanics [Titscher et al. 2019], which is advantageous as it seamlessly integrates into continuum finite element codes.

2.2.2 Continuum damage mechanics

The term *continuum damage mechanics* is first mentioned in [Kachanov 1958] and describes material deterioration, in contrast to classic fracture mechanics[1] in a continuous, smeared fashion [Simo et al. 1987; Kachanov 2013]. The influence of defects on the material is modeled by field variables, most dominantly *damage*, that then modify the elastic properties of the material. A value of zero indicates virgin, intact material and corresponds to the purely elastic material response. Microcracks are not able to transmit the same forces as intact material. On the microscale, this corresponds to a reduction of effective, load-carrying cross chapter of the material. The damage variable can be interpreted as the fraction of cracked surface, projected onto the loading direction. Complete material failure occurs for a damage value of one and the material shows no more resistance to external loads.

In the most general case, the damage variable is a fourth order tensor. The experimental identification of all its components, however, is extremely difficult. Thus, a symmetric second order tensor is more commonly used [Sidoroff 1981; Carol et al. 1997].

Isotropic damage models

Defining the damage variable as a scalar value removes the directional information and leads to isotropic damage models. But some of the directional information is recovered in a spatial sense. A uniaxial tensile loading results in a narrow damaged band that reduces the body's stiffness in loading direction. In a perpendicular direction, however, the *projected* load-carrying cross-chapter is only reduced by the width of the damaged zone. If that zone is sufficiently small compared to the body's dimensions, it merely influences the material behavior in that direction.

The stored energy density of such a model reads

$$\psi = (1 - \omega)\psi_0 = (1 - \omega)\frac{1}{2}\boldsymbol{\varepsilon} : \boldsymbol{C} : \boldsymbol{\varepsilon}, \tag{2.1}$$

where $0 \leq \omega < 1$ denotes the scalar damage variable and ψ_0 is the elastic energy density. The latter one is written in terms of the fourth-order elasticity tensor $\boldsymbol{C}$ and the second-order strain tensor $\boldsymbol{\varepsilon}$.

---

[1]Phase field models for brittle failure [Miehe et al. 2010; Ambati et al. 2015] reformulate the crack description in a continuous way.

Implications for the damage growth and the constitutive modeling are derived from the dissipation inequality mentioned above. In a local form and for a constant temperature [Jirásek et al. 2002b] it reads

$$\dot{\mathcal{D}} = \boldsymbol{\sigma} : \dot{\boldsymbol{\varepsilon}} - \dot{\psi} \geq 0, \tag{2.2}$$

where $\boldsymbol{\sigma}$ is the second-order stress tensor. After inserting Eq. (2.1),

$$\dot{\mathcal{D}} = (\boldsymbol{\sigma} - (1 - \omega)\boldsymbol{C} : \boldsymbol{\varepsilon}) : \dot{\boldsymbol{\varepsilon}} + \psi_0 \, \dot{\omega} \geq 0 \; \forall \dot{\boldsymbol{\varepsilon}} \tag{2.3}$$

follows. Without limiting the choice of $\dot{\boldsymbol{\varepsilon}}$, this inequality can only be fulfilled for

$$\boldsymbol{\sigma} = (1 - \omega)\boldsymbol{C} : \boldsymbol{\varepsilon}, \tag{2.4}$$

which represents the constitutive equation, in this case Hookes law, reduced by the factor $(1 - \omega)$.

With the positive potential ψ_0, the dissipation inequality can only be fulfilled for a non-negative damage growth. So even for unloading conditions, the damage must not decrease. This implies that the damage variable cannot directly depend on the stresses or strains. Instead, an additional history variable κ is introduced that captures the historic maximum of the damage driving variable. Acounting for the maximum dissipation principle [Simo et al. 2006], this is formulated by the loading-unloading conditions

$$f \leq 0, \quad \dot{\kappa} \geq 0, \quad \dot{\kappa}f = 0, \tag{2.5}$$

with the loading function f, usually in the form

$$f(\kappa, \varepsilon_{\text{eq}}) = \varepsilon_{\text{eq}} - \kappa. \tag{2.6}$$

Here, ε_{eq} denotes an equivalent strain measure as the damage driving variable.

The exact shape of the post-peak curve or softening curve is defined by a damage law $\omega(\kappa)$. For the isotropic case, that is a scalar function that monotonically depends on the history variable to ensure non-negative damage growth. The two material parameters that commonly define the damage law are the tensile strength f_t and the fracture energy G_f. They can directly be determined by an uniaxial tensile test. Equation (2.4) for this case is shown schematically in Fig. 2.3 for an exponential damage law [Mazars et al. 1989; Oliver et al. 1990]. The tensile strength is the peak load at the point of damage initiation and the fracture energy is related to the integral of the curve.

The definition of the equivalent strain measure heavily influences the model's behavior as they determine the boundaries of the elastic domain. They are defined by a loading function that, in the simplest case, leads to damage growth when the equivalent strain exceed a threshold. As illustrated in Fig. 2.3, this defines the maximal material strength. A definition of the equivalent strains as the simple Euclidean or energy norm leads to almost equal material strength in all loading directions. A Rankine failure criterion
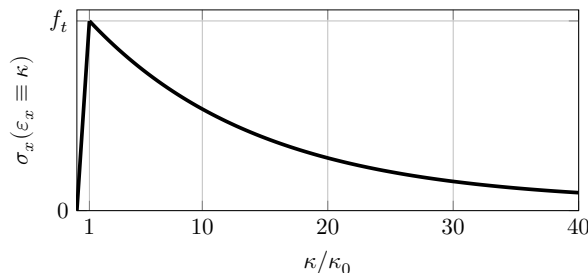
Figure 2.3: Uniaxial tensile test with an exponential damage law.

corresponds to unlimited compressive strength. Both versions are in contrast to the experimental observation that the compressive strength of concrete is about one order of magnitude higher than its tensile strength [Kupfer et al. 1969]. This is modeled with the modified von Mises formulation. It introduces a scalar factor that expresses the ratio of the materials compressive strength and its tensile strength [Vree et al. 1995].

These models cannot capture the correct strength envelopes, especially in biaxial loadings. A remedy is to introduce a split into one damage variable for compression, one for tension, with separate and more complex loading functions [Mazars 1986; Comi et al. 2001]. Another problem with isotropic damage models is the crack closure effect, also referred to as unilateral stiffness recovery. Cracks that correctly reduce the materials stiffness in tension close in compression. The contacting crack faces can transmit compressive stresses similar to the virgin material. In a simplified approach, this effect can be modeled by splitting the elastic law into a hydrostatic and deviatoric components and omit damaging the compressive hydrostatic part. A more sophisticated formulation that also affects the deviatoric part is achieved by selectively deactivating damage in a principal component split [Ladeveze et al. 1984; Faria et al. 1998].

Multiphysics coupling

In pure damage formulations, or elasto-damage formulations, the defects close perfectly and the stress-strain curve unloads to the origin, as depicted by the dotted line in Fig. 2.4. The effective stiffness is permanently reduced.

Plastic materials are characterized by a permanent deformation. In unloading, the deformation in form of a plastic strain remains in the load-free state. The stiffness of the virgin material is not affected. This is illustrated with the dashed line in Fig. 2.4.

Plastic models consist of a yield surface, a flow rule and a hardening law. The yield surface, similar to the loading function in damage models, defines the boundary of the elastic regime. In the Mises- or $J2$-plasticity this yield surface is defined in terms of the second deviatoric stress invariant [Mises 1913]. A pressure-sensitive formulation is achieved by adding the first invariant, e.g. in the Drucker-Prager yield surface [Drucker et al. 1952].
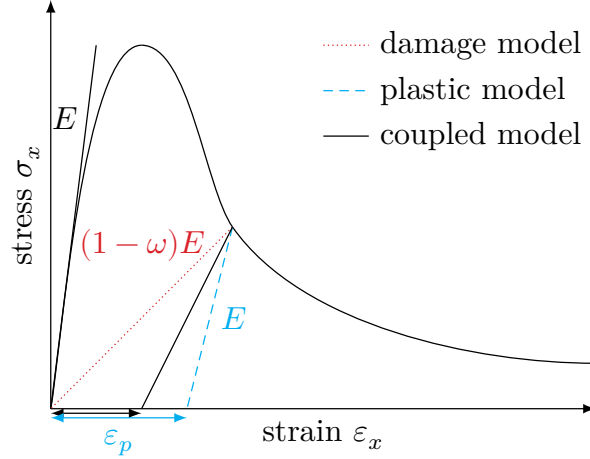
Figure 2.4: Unloading paths for different softening material models.

For concrete, the formulations also include the third deviatoric invariant [Ottosen 1977; Menetrey et al. 1995] or multiple yield surfaces [Feenstra et al. 1996]

The flow rule defines the evolution of plastic strains, once the stress state reaches the yield surface. In associative flow rules, plastic strains grow normal to the yield surface, which is well-suited for metals. For pressure-sensitive materials like concrete, an additional, non-associative flow rule has to be defined [Pramono et al. 1989].

The plastic flow leads to microstructural changes that influence the initial yield surface. Its evolution is described by the hardening law. Isotropic hardening changes its size, kinematic hardening its position and mixed formulations modify both [Lubliner 2008].

The coupling of damage and plasticity, e.g. [Grassl et al. 2006; Unger et al. 2011a], is achieved by introducing the plastic strains $\boldsymbol{\varepsilon}_p$ into Eq. (2.4)

$$\boldsymbol{\sigma} = (1 - \omega)\boldsymbol{C} : (\boldsymbol{\varepsilon} - \boldsymbol{\varepsilon}_p) \tag{2.7}$$

and results in both a loss of stiffness and permanent deformations (see solid line in Fig. 2.4). The effects of temperature are similarly introduced by adding additional thermal strains and hygroscopic models add the contribution of the pore pressure via shrinkage strains [Gawin et al. 2007]. Even though this work focuses purely on damage modeling, the straight-forward inclusion of multiphysics phenomena, possibly in future works, justifies the use of continuum damage models for both quasistatic and fatigue simulations.

2.3 Fatigue modeling

Fatigue failure describes the material deterioration or fracture under cyclic loads that can be well below the quasistatic failure limits. The experimental works on fatigue of
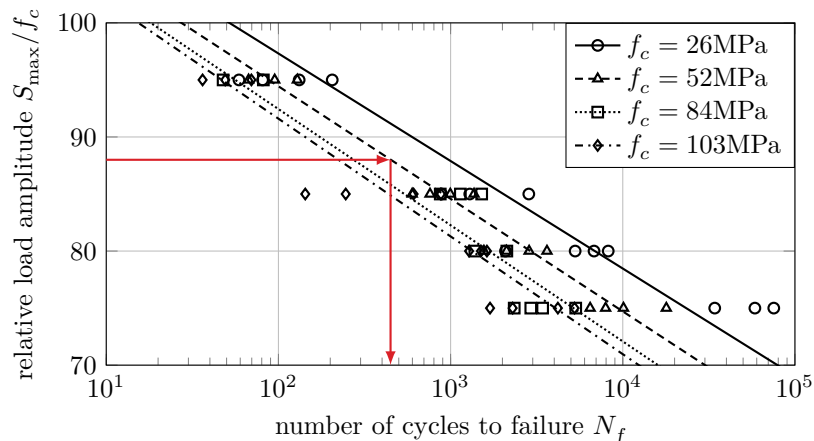
Figure 2.5: Wöhler lines of cylindrical concrete specimen under compressive loading from [Kim et al. 1996].

concrete go back to the early 1900s and deal with the ultimate material failure [Murdock 1965]. For a given load amplitude S_{max}, the number of loading cycles until material failure N_f is measured. This is done for multiple load amplitudes and results in S-N-curves or Wöhler curves, as shown in Fig. 2.5.

They can be used for a basic structural dimensioning. A linear elastic simulation identifies the highest *local* load in a critical part of the structure. As indicated by the arrows in Fig. 2.5, this load is then used to determine the expected cycles to failure from the corresponding Wöhler lines of the material.

Figure 2.5 also shows a difference of up to one order of magnitude in the resulting value of N_f. This high variance occurs even though the test specimens were manufactured from the same batch of concrete. The Wöhler lines are not only influenced by the material parameters. The long run time of the experiments influences the material behavior, because the impact of long-time effects such as creep or shrinkage is significantly higher as for quasistatic experiments. Other influences are the specimen size [Bažant et al. 1991], its age [Raithby 1979] and the loading frequency [Medeiros et al. 2015]. This results in enormous experimental efforts to create Wöhler curves for all combinations of influences.

Thus, to gain a better understanding of the effects of each phenomenon and its impact on the overall failure, the experimental efforts shift towards investigating the whole failure process instead of the single point of failure [Thiele 2015]. Non-destructive in-situ techniques like digital image correlation [Mahal et al. 2015] or the measurement of acoustic emissions [Noorsuhada 2016] help to characterize the failure process. The underlying effects that cause fatigue failure, however, remain not fully understood [Sinaie et al. 2015].

The modeling of the whole failure process requires material models that allow material

Thomas Titscher

deterioration under cyclic loading. They should automatically resolve stress redistributions over the life time, can model arbitrary load shapes and amplitudes and can lead to a deeper understanding of the processes that lead to fatigue failure.

A modeling approach is to express the loading function (Eq. (2.6)) and loading-unloading conditions (Eq. (2.5)) in an incremental form

$$\dot{\kappa} = \begin{cases} \dot{\varepsilon}_{\text{eq}} & \text{if } \varepsilon_{\text{eq}} = \kappa \\ g & \text{if } \varepsilon_{\text{eq}} < \kappa. \end{cases} \tag{2.8}$$

A fatigue function g is introduced that represents the quasistatic model for $g \equiv 0$. For $g > 0$, however, Eq. (2.8) allows damage accumulation within the elastic regime [Marigo 1985][2]. Formulations for g can be derived from cohesive zone models [Kuna et al. 2015]. More sophisticated models are not only based on damage but include plasticity [Sima et al. 2008; Breccolotti et al. 2015] or creep [Kindrachuk et al. 2015].

The focus of this work is the numerical treatment of the model and not the model itself. Thus, a basic fatigue model with

$$g = \left(\frac{\varepsilon_{\text{eq}}}{\kappa}\right)^n \langle \dot{\varepsilon}_{\text{eq}} \rangle_+ \tag{2.9}$$

is used [Marigo 1985; Fish et al. 2002; Fish et al. 2012; Kindrachuk et al. 2018]. The Macaulay brackets denoted by $\langle \ \rangle_+$ correspond to the ramp function and prohibit a damage accumulation in unloading conditions. The exponent n is the only free parameter and usually not sufficient for a calibration to experimental data. This formulation, however, automatically includes the quasistatic case for $\varepsilon_{\text{eq}} = \kappa$.

---

[2]The third option $g < 0$ violates the dissipation inequality.

3 Computational aspects of concrete modeling

The available computational power continuously increases and enables larger and more detailed numerical simulations. This trend is often described by Moore's law, the observation that the number of transistors in integrated circuits doubles every 24 months. This influences the computational performance to also grow exponentially. The growth of single core performance, however, started to slow down since 2000. This is commonly compensated by distributing a single simulation to multiple cores. In the case of high-performance computing, millions of cores available in supercomputers can be utilized. But even modern workstations provide multiple cores that can be used to increase the level of detail or decrease the run time of simulations.

The efficient utilization of available computational power requires domain decomposition techniques to parallelize the problem and are itself a huge area of research [Toselli et al. 2006]. Especially for softening materials, the numerical effort required in each domain depends on its continuously evolving damage state and requires load balancing algorithms [Willebeek-LeMair et al. 1993]. Additionally, the increasing computational power leads to an increased environmental cost. As of June 2019, the *Summit* leads the Top500 supercomputer ranking [Top 500 2019] with a power consumption of 13 MW, which results in a significant amount of carbon dioxide emissions.

These factors motivate the work on methods that reduce the computational costs instead of increasing the computational power.

3.1 Sphere packing for mesoscale simulations

In this work, sphere packing algorithms are used to place the aggregate particles of the concrete mesostructure into a virtual specimen. A given specimen volume and a required particle volume fraction determine the actual particle volume. A list of spheres diameters is randomly sampled according to the grading curve of Section 2.1 until the required particle volume is reached. The details of this procedure are shown in chapter 2 of Paper 1. It turns out that the simple process of *pouring* these particles into a container is a challenging algorithmic task, solved with packing algorithms.

3.1.1 Sphere packing algorithms

Spheres packings describe the arrangements of non-overlapping spheres in a given domain. An interesting question is to determine the configuration that maximizes the sphere density ϕ, also referred to as their volume fraction. This density describes the proportion of space filled by them.

The optimal packing of equal spheres was first investigated in the 16th century in the context of cannonball stacking. The maximal volume fraction of $\phi_{\max} \approx 74.05\%$ was formulated in the Kepler conjecture and only recently proven [Hales 2005]. This corresponds to a regular lattice in either hexagonal close-packed (hcp) or face-centered cubic (fcc) configuration. Due to the complexity of bidisperse or polydisperse sphere packings, the problem is often investigated numerically [Torquato et al. 2010]. But the packing of equal spheres remains relevant for crystal forming processes, as a benchmark problem for the used algorithms [Titscher et al. 2015] or for packings in higher dimensions [Skoge et al. 2006]. Interestingly, randomly arranged spheres form a maximally random jammed packing (MRJ) and only reach $\phi_{\mathrm{MRJ}} \approx 64\%$ [Kansal et al. 2002a]. Unlike the long-range ordering of hcp and fcc, the spheres form optimally packed clusters in varying orientations, resulting in short-range ordering with lower space-filling.

The variety of existing sphere packing algorithms and their applications are discussed in the introduction of Paper 1. Two main categories are identified, namely fixed and moving particle algorithms. Fixed particle algorithms keep the position and size of placed particles constant. One example of this category is the random sequential addition (RSA) algorithm [Widom 1966], where a particle is placed randomly, if it does not overlap with previously placed ones.

This will always result in a small gap between particles that result in a loosely packed state. These gaps remain even for more sophisticated algorithms that construct the next particle position to touch existing ones. Figures 3.1a and 3.1b illustrate this problem. However, these algorithms are commonly used for the creation of concrete mesostructures [Bažant et al. 1990; Wriggers et al. 2006] and can be extended for non-spherical particles [Wang et al. 1999; Häfner et al. 2006; Unger et al. 2011a].

Moving particle algorithms often resemble molecular dynamics (MD) phenomena and allow rearrangements of the particles. In time-driven MD, e.g. [Cundall et al. 1979], a system of motion equations is solved explicitly. Separation forces between overlapping particles causes them to separate in the next time step. Close to the jammed state, these forces may not be sufficient to prohibit overlaps. Event-driven molecular dynamics (EDMD) was first introduced for efficient simulations of molecule interactions in dilute systems [Alder et al. 1959]. All particles in the system are constantly moving via free-flight dynamics and collisions between them or with the walls are fully elastic.

The extension of this algorithm to growing particles allows to reach a random close packing of discs in 2D [Lubachevsky et al. 1990]. The advantage of this approach is

(a) Randomly placed parti-
cles (solid) are not al-
lowed to move. They
block all positions for
new (dashed) particles.

(b) The same effect as in (a)
occurs if the fixed parti-
cles are placed not ran-
dom but close to walls
and other particles.

(c) Particle movement al-
lows a rearrangement to
fit all particles.
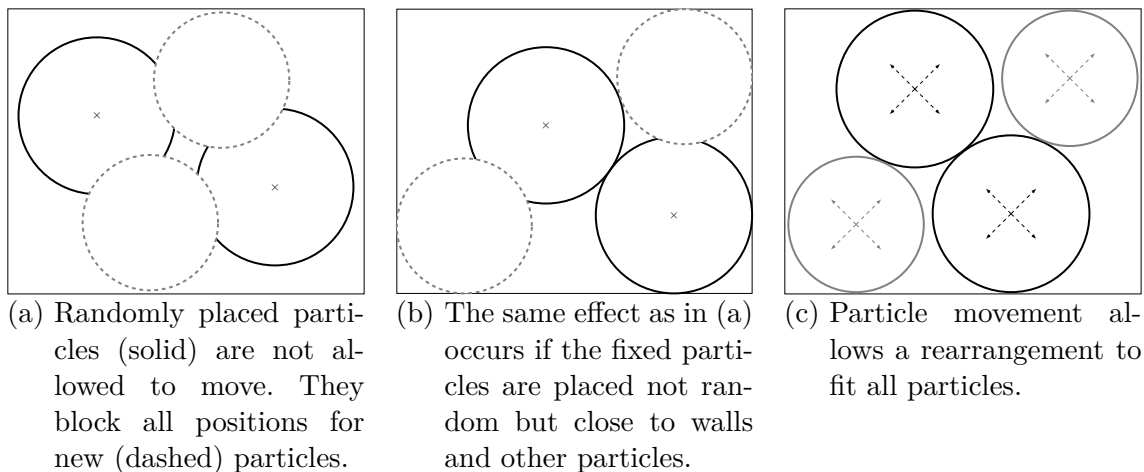
Figure 3.1: Main advantages of moving particle methods over fixed ones at high particle
volume fractions ϕ.

shown in Fig. 3.1c. A different growth rate for each particle results in bidisperse [Kansal
et al. 2002b] or polydisperse [Baranau et al. 2014] packings. And the handling of non-
spherical shapes is briefly discussed in chapter 7 of Paper 1.

Due to the high efficiency of RSA algorithm at rather low volume fractions, it is com-
monly used as the initial configuration of the EDMD algorithm. This technique is also
employed in this work and both algorithms are briefly introduced.

3.1.2 Random sequential addition

All particles are sorted according to their volume and the placement process is started
with the largest particle. Uniform random numbers are generated for all coordinates. In
the case of cuboid specimens, boundary overlaps are eliminated by the right choice of the
random number interval. Other specimen shapes such as cylinders require an additional
boundary collisions check.

The overlap check with already placed particles is done by a simple sphere separation
check. If the particle overlaps with previously placed particles, a new random position
is chosen. After a certain number of failed placement attempts of a single particle, the
algorithm aborts.

The complexity of the collision checks of a single particle is $\mathcal{O}(N)$, since it must be
checked against all already placed particles. The *Big O notation* describes the asymptotic
behavior of an algorithm up to a constant factor, in this case a linear dependency on
the number of particles N. This assumes that all the particles are assigned to a big
list that needs to be traversed for the overlap checks. The particle position, however,

offers additional information that is used by spatial data structures for a tremendous performance increase[1]. Here, the cell method or subbox method is used. The specimen is divided into multiple cells and any given position is directly related to one of the cells. The collision checks are now only performed within the cell of the current particle. As the number of cells is related to the number of particles, a constant number of collision checks ($\mathcal{O}(1)$) eliminates overlaps.

3.1.3 Event-driven molecular dynamics

At the start of the EDMD algorithm, the specimen must already contain all particles. This initial packing is trivial for zero-sized particles or low particle volume fractions. A random initial velocity and a growth rate is given to each particle and the system evolves in time. The growth rate of each individual particle is defined such that it reaches its final diameter after a given simulation time t_{end}. Consequently, the resulting size distribution is in accordance with the desired grading curve.

The evolution of the system is then defined in terms of discrete events instead of a continuous time. Each event describes the collision of a particle with either another particle or the specimen wall at a certain time. These events are collected in an event list that is sorted by time. The time is then advanced to the time of the nearest future event and an elastic collision of the two *collidables* is performed. This changes their velocity and, thus, invalidates all their future events. They have to be deleted from the event list and new events have to be predicted.

The high number of collision checks and the maintenance of the event list are the main numerical cost. The corresponding complexities are further discussed in chapter 5.4 of Paper 1, together with state-of-the-art optimization techniques. One of them is the previously mentioned subbox method. A novel optimization technique is the time barrier. In simple words, it ignores all events that are after a well defined future point in time which reduces the size of the event list. Once the time barrier is reached, a new one is chosen and the event list is fully rebuild.

3.1.4 Applications and results for the concrete mesostructure

Concrete grading curves are commonly defined for size classes up to 32 mm and down to 0.125 mm. That means that some aggregates even pass the finest sieve. Including them in the mesostructure leads to an amount of aggregates that can neither be handled by the sphere packing algorithms, nor the subsequent mesh creation, nor the final finite element simulation. In concrete geometry simulations, a common choice for the cutoff diameter

---

[1]Spatial data structures are also widely used in computational mechanics to efficiently find elements in a given mesh, e.g. for node selection or tracking of embedded discontinuities [Unger 2009].
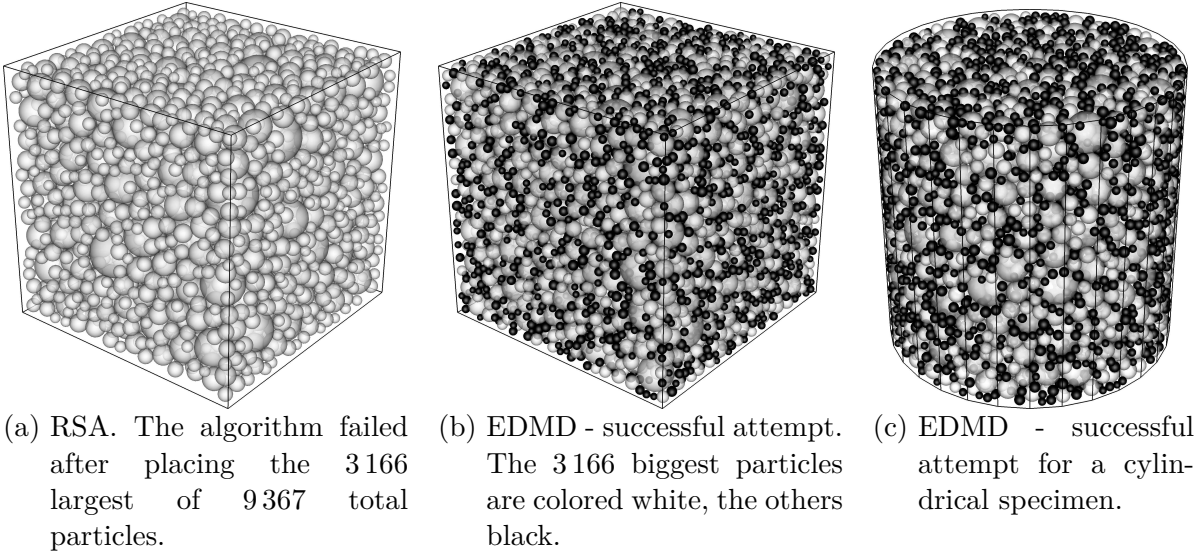
(a) RSA. The algorithm failed after placing the 3 166 largest of 9 367 total particles.

(b) EDMD - successful attempt. The 3 166 biggest particles are colored white, the others black.

(c) EDMD - successful attempt for a cylindrical specimen.

Figure 3.2: Result of the simulation with $a = 5\ d_{\mathrm{max}}$ and an effective volume fraction of $\phi_{\mathrm{eff}} = 70\%$.

is $d_{\mathrm{min}} = 2$ mm [Unger et al. 2011a]. All particles smaller than 2 mm are sand grains that are assumed to be represented by the homogenized mortar matrix. Their volume is subtracted from the total volume and the effective volume fraction ϕ_{eff} reduces. In the common case of a mixture volume fraction $\phi_M = 70\%$, which represents the aggregate volume fraction that is physically filled into the concrete mixer, and the grading curve B16 [DIN 1045 2008], the volume fraction that is actually resolved by the mesoscale geometry model is $\phi_{\mathrm{eff}} = 40.6\%$.

With this in mind, the performance of the RSA and the EDMD algorithm is compared. As expected by the discussion on fixed vs. moving packing algorithms, EDMD performs better. It is able to fill 70% of the specimen, whereas the RSA algorithm already fails at 66.5%. The particle distribution for $\phi_{\mathrm{eff}} = 70\%$ is illustrated in Fig. 3.2. The RSA algorithm stopped after placing 3 166 of 9 367 particles, whereas the EDMD was successful.

Another problem is related to the meshing of the generated particle geometries and the subsequent simulation using finite elements. For numerical reasons, highly distorted elements should be avoided. For this purpose, a minimal distance Δd between any two particles is enforced. This is done by adding Δd to each particle diameter during the sphere packing and removing it afterwards. Obviously, this highly influences the particle distribution. In this configuration, the EDMD algorithm reaches an 11% higher particle volume fraction.

In the case of growing particles in the EDMD algorithm, the grading curve is exactly matched at t_{end}. Even if the specimen had room for further particle growth, the resulting distribution would differ from the desired grading curve. So, in the previously shown experiments, the algorithm was always stopped at t_{end}. The distance between the

particles, however, is removed after the simulation and does not influence the effective distribution. Here, the EDMD algorithm excels, as it can maximize Δd until a jammed state is reached. For a B16 grading curve and the desired 70% mixture volume fraction, it is always able to reach a minimal particle distance $\Delta d > d_{\min}/2..$

3.2 Computational damage mechanics

The material descriptions sketched in Section 2.2.2 lead to (a system of) partial differential equations (PDE). Analytic solutions exists for a few crafted cases, but generally, they have to be solved numerically, e.g., with the finite element (FE) method [Hughes 2012].

The details of the method are common knowledge, but a sketch is given here to introduce the terminology used. The PDE is expressed in variational form and its solution is approximated by finite sized elements that provide the solution values at their nodes and interpolate between them. Linear elements have the node positions at their corners and interpolate their values linearly. A better approximation of the solution is obtained for higher order elements that introduce additional nodes within the element or at its edges or faces. The discretization of the continuous problem to a discrete one in terms of nodal positions leads to a residual vector that has to be equilibrated. This root-finding problem can be solved with the Newton-Raphson algorithm that requires tangent stiffness matrix which is the derivative of the residual vector with respect to the nodal values. The details of this scheme in combination with a line-search algorithm for additional stability are shown in chapter *Backward Euler Time Integration* of Paper 2.

3.2.1 Localization and regularization

The finite element solution of softening models, like the ones presented in Section 2.2.2 is known to suffer from mesh sensitivity. This is caused by a loss of ellipticity of the equilibrium equations [Bažant 1976; Vree et al. 1995]. It results in a dependency of the solution on the underlying finite element mesh in two main categories. First, the numerical solution converges to a non-physical solution upon mesh refinement. Second, the localization path that approximates the macroscopic cracks depends on the mesh orientation. The root of these problems is the inability of the finite element mesh to resolve the present characteristics of the problem. And for softening materials, these characteristics correspond to a discrete crack that cannot be resolved in a continuous volume.

Mathematically, this problem is addressed in the localization analysis [Hill 1958]. The goal is to define conditions on how a continuous strain field transforms into narrow bands with a strain jump. This can be analyzed for a given model in terms of critical damage

values and localization angles [Jirásek 2007]. The main problems that lead to the mesh dependency, however, can also be illustrated in a simple one dimensional bar.

A homogeneous one dimensional bar is loaded in uniaxial tension. The momentum balance equation implies a uniform stress that grows elastically until the material's tensile strength is reached. Further pulling on the bar causes the stresses to reduce, according to the softening law, see Fig. 2.4. Every cross chapter of the material can now have two possible strain states. In one fraction of the bar, the strains decrease and the reduced stress is reached by an elastic unloading. The remaining part of the bar exhibits increased strains and a damage-based stress drop. The damaged fraction of the bar, however, is undetermined and every value fulfills the governing equations.

Real materials are not perfectly homogeneous and exhibit small variations in their properties. The part of the bar with the lowest tensile strength will damage first and localize. As the tensile strength of the other parts of the bar is not reached, they unload elastically. The overall material behavior now depends on the size of the weakest zone.

The fracture energy is a material property that describes the energy required to generate stress-free crack surfaces within the material. It is a parameter in continuum damage models, usually used within the damage law. Continuum models have no description of an internal surface and the fracture energy is dissipated over a volume. So a larger softening zone dissipates more energy than a smaller zone, and an infinitely small zone dissipates no energy. In a simulation of the bar with linear finite elements, the minimal zone size is defined by the finite element size. Thus, the localization occurs within a single finite element and the dissipated energy depends on its size [Sluys et al. 1992; Jirásek 1998].

One of the possible remedies to this problem is to include the width of the finite element in the constitutive relationship. This was first done in softening plasticity [Pietruszczak et al. 1981] and later adapted to damage modeling [Bažant et al. 1985]. The idea is to spread the displacement jump of the traction-separation law into a localized strain band with a defined size. The transformation of the tractions to continuous stresses is adapted accordingly. This leads to a simple scaling of the constitutive parameter that controls the softening behavior and is easy to add in existing finite element codes. These models are referred to as crack band models or models with mesh-adjusted softening modulus.

Problems arise in two or three dimensions where the definition of the localized band size is not clear. If the crack is oriented parallel to the sides of a regular, quadrilateral finite element mesh, the crack band size equals the edge length of the finite elements. This leads to the common approximation of the characteristic element length as the square root its area (2D) or the cubic root of its volume (3D). This changes for inclined cracks [Bažant 1985] and the band size is related to the assumed crack path [Oliver 1989], often determined by the direction of principal strains. Strain-injection methods can then be employed to obtain a localization path that is not disturbed by the mesh orientation [Dias et al. 2018].

Additional care has to be taken for higher order elements, as they can resolve a crack band that is smaller than their size. In the one-dimensional case, the effective band width can be adapted accordingly, but simulations in multiple dimensions require further adaptions, especially if the localized zone is not aligned with the mesh. Further challenges occur, e.g. for deviations from pure uniaxial stress states and localization near symmetry planes. This is further discussed in [Jirásek et al. 2012].

Nonlocal damage models

The previously discussed models can be labeled as *local* models as the stresses at one position of the body are directly calculated by the strains there. This is advantageous for finite element simulations, since the elements can be evaluated separately. The mesh-adjusted softening modulus improves the objectivity of numerical results, especially the mesh-insensitive dissipated energy in uniaxial loading. But the localization still occurs within a single layer of elements and the problems described above remain.

More sophisticated techniques enrich the continuum formulation with additional information regarding the internal material structure. They aim to enforce a mesh-independent size of the localized zone. Examples are Cosserat theories that introduce additional rotational degrees of freedom [Cosserat et al. 1909] and viscoplastic regularization techniques that introduce rate-dependent terms [Needleman 1988]. They are further discussed with other alternatives in [Bažant et al. 2002]. The two classes of nonlocal integral models and gradient enhanced models are further discussed here.

Nonlocal integral models [Pijaudier–Cabot et al. 1987] generally replace a local function with its weighted average over a volume V. Several nonlocal models are reviewed and compared in [Jirásek 1998] that differ in the choice of the local function. A formulation, where damage is driven by an averaged equivalent strain $\varepsilon_{\mathrm{eq}}$, convergences upon mesh refinement, while this is not the case for formulations that directly average the damage or the strains. The corresponding nonlocal equivalent strain formulation reads

$$\bar{\varepsilon}(\boldsymbol{x}) = \int_V \alpha(\boldsymbol{x} - \boldsymbol{\xi})\varepsilon_{\mathrm{eq}}(\boldsymbol{\xi})\mathrm{d}\boldsymbol{\xi} \tag{3.1}$$

where α denotes the nonlocal weight function. It is typically formulated in terms of the distance $r = \|\boldsymbol{x} - \boldsymbol{\xi}\|$ of the source point $\boldsymbol{\xi}$ to the target point $\boldsymbol{x}$, e.g. in a Gaussian distribution function. This function includes the internal length l that controls the radius of the nonlocal interaction.

The nonlocal equivalent strains $\bar{\varepsilon}$ are included in the model by replacing the local equivalent strains in the loading function (Eq. (2.5)) with their nonlocal counterpart

$$f(\kappa, \bar{\varepsilon}) = \bar{\varepsilon} - \kappa. \tag{3.2}$$

Compared to the crack band regularization, this technique requires major changes in the

implementation, as the finite elements can no longer be evaluated separately. The contribution of each element consists of all other elements. Practically, the weight function is limited to a certain radius R and the averaging is restricted to elements within R. In a naive implementation, even this neighbor search can be a bottleneck for large FE meshes, but spatial data structures as sketched in Section 3.1.2 solve this problem. The bigger numerical problem is the structure of the tangent stiffness matrix. In the undamaged state, it corresponds to a linear elastic model where the bandwidth of the matrix is determined by the direct neighbor elements. This sparsity pattern remains constant in a local formulation. As damage evolves in an integral nonlocal formulation, the bandwidth of the matrix grows. This requires dynamic memory allocations and decreases the numerical solver performance [Jirásek et al. 2002a]. Especially for concrete on the mesoscale that shows distributed damaged zones, this approach has a high numerical cost.

A nonlocal gradient formulation based on equivalent strains, namely the implicit gradient-enhanced damage model, can be derived from Eq. (3.1) with a Taylor expansion of $\varepsilon_{\mathrm{eq}}(\boldsymbol{\xi})$ [Peerlings et al. 1996]. This approximation results in the boundary value problem

$$\bar{\varepsilon} - l^2 \nabla^2 \bar{\varepsilon} = \varepsilon_{\mathrm{eq}} \text{ in } V \text{ and} \tag{3.3}$$

$$\nabla \varepsilon_{\mathrm{eq}} \cdot \boldsymbol{n} = 0 \text{ on } \partial V \tag{3.4}$$

that has to be solved in addition to the momentum balance equations. In fact, this model is equivalent to a nonlocal integral model with the Green's function of Eq. (3.3) as the weighting function [Peerlings et al. 2002].

The same equations can be derived in a thermodynamically consistent way from the free energy potential

$$\psi(\boldsymbol{\varepsilon}, \varepsilon_{\mathrm{eq}}, \omega) = \frac{1}{2}(1 - \omega)\boldsymbol{\varepsilon} : \boldsymbol{C} : \boldsymbol{\varepsilon} + \frac{1}{2}h(\varepsilon_{\mathrm{eq}} - \bar{\varepsilon})^2 + \frac{1}{2}hl^2 \nabla \bar{\varepsilon} \cdot \nabla \bar{\varepsilon}, \tag{3.5}$$

which is further shown in chapter *Governing Equations* of Paper 2. The first term of Eq. (3.5) is already known from the stored energy density of a local damage model in Eq. (2.1). The second term describes the stored energy between a nonlocal strain field $\bar{\varepsilon}$ and a local strain norm $\varepsilon_{\mathrm{eq}}$. The parameter h can be interpreted as a local-to-nonlocal coupling modulus. The third term includes the energy of gradients of the nonlocal strain field and the nonlocal length parameter l.

The localization analysis of the gradient-enhanced damage model proves that it remains well-posed [Peerlings et al. 2002]. This is caused by the screened Poisson equation in Eq. (3.3) that limits the curvature of the nonlocal equivalent strain field $\bar{\varepsilon}$ and prohibits full localization. The main additional numerical cost is the introduction of the nonlocal strains $\bar{\varepsilon}$ as an additional scalar degree of freedom that increases the size of the resulting system of equation. In contrast to the integral formulations, the band structure remains narrow and is known a priori.
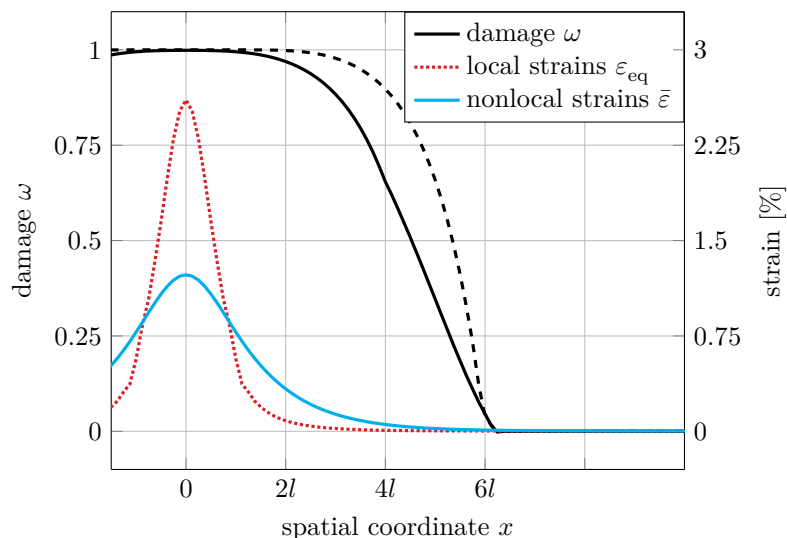
Figure 3.3: Behavior of the gradient-enhanced damage model in a uniaxial tensile test. The dashed line corresponds to the damage profile after doubling the boundary displacement.

Figure 3.3 shows a typical damage plot of the gradient-enhanced damage model, where the peak damage reaches the value $\omega \approx 1$. The distribution of the local strain norm is higher and narrower than that of its nonlocal counterpart. A geometric notch is introduced in the form of a 10% reduced cross chapter at $x \in [-l, l]$ to trigger the localization. This explains the small kink in the local strain norm. The characteristics of the damage law cause the damaged zone to be much wider than the nonlocal strain zone. In this sense, it really describes a zone of distributed microcracks where only values very close to one represent a localized crack.

Note that the nonlocal length l is not directly related to the width of any of the shown variables. So even if the actual characteristic length is known from experiments [Bažant et al. 1989; Geers et al. 1996], the model parameter l has to be calibrated such that the localized zone sizes of model and experiments match. This is done once for a given material and the calibrated l corresponds to a constitutive parameter of the model. This is an advantage over the regularization techniques of local models where the characteristic length can vary for each element and Theoretically depends on the current stress state of the structure, which is often neglected due to computational reasons.

The additional dashed line in Fig. 3.3 shows the damage distribution after further increasing the boundary displacement. This causes the local strains to grow further. As the curvature of the nonlocal strains is limited by Eq. (3.3), their distribution widens and damage continues to grow. This spurious damage growth in fully localized regions is one of the disadvantages of the gradient-enhanced damage model. Another one is a deficiency regarding damage initiation in shear problems [Simone et al. 2004]. Both problems are addressed by using a nonlocal length parameter that decreases with growing

local strains [Saroukhani et al. 2012] or with damage [Poh et al. 2017]. That way, with a vanishing nonlocal length, the model transitions towards a local model. Obviously, a certain fraction of the initial nonlocal length is needed for the problem to remain well-posed. This imposes constraints to the mesh where the element length has to be reduced significantly to resolve the narrower nonlocal zone.

The interpolation order of the nonlocal strain field $\bar{\varepsilon}$ is originally chosen to be one order lower than the displacement field $\boldsymbol{d}$ [Peerlings et al. 1996]. That way, the local strain norm calculated as the spatial derivative of $\boldsymbol{d}$ has the same interpolation order as $\bar{\varepsilon}$. This restriction, however, is no requirement and any combination of interpolation orders can be used [Simone et al. 2003]. In chapter *Appendix* of Paper 2, this was analyzed up to order four and equal interpolation orders perform best.

3.2.2 Instabilities

The term instabilities is used here to generally describe numerical problems that arise in the solution of the global system of equations. One such instability is the snap-back phenomenon that occurs in certain configurations where the stored elastic energy spontaneously dissipated. Sophisticated loading methods like arc-length methods [Riks 1979; Geers 1999a; Geers 1999b] or dissipation based loading [Verhoosel et al. 2009; May et al. 2016] solve this issue globally. Within a mesoscale geometry, however, this can occur locally between aggregates. This results in mini-snapbacks that barely influence the global behavior but require tiny load increments to resolve.

Another problem are structural bifurcations. A simple example is a symmetric structure under bending with only one aggregate. As the damaged zone reaches the aggregate, both the left or the right continuation are possible. This also results in tiny load increments, until the point, where one path is chosen. Note that the global response is identical for both paths.

For a sufficiently complex mesoscale structure, both phenomena contribute to a bad performance of classic backward Euler solution schemes, i.e. the common linear Taylor expansions and the Newton-Raphson solution of the governing equations that is described in detail in chapter *Backward Euler Time Integration* of Paper 2. In a three-dimensional mesoscale simulation, the solution in Fig. 3.4 required 259 adaptive load increments and 1100 solutions of the global system of equations. The details of this simulations are presented in chapter *Three-dimensional Compression Test* of Paper 2.

Numerical methods to address these issues were first applied to local damage models, like the continuous strong discontinuity approach used in this work. A singular acoustic tensor of these models corresponds to zero eigenvalues in the element stiffness matrices. Through the assembly process of all elements of the finite element mesh, even the global algorithmic tangent matrix can become ill-conditioned [Oliver et al. 2006].

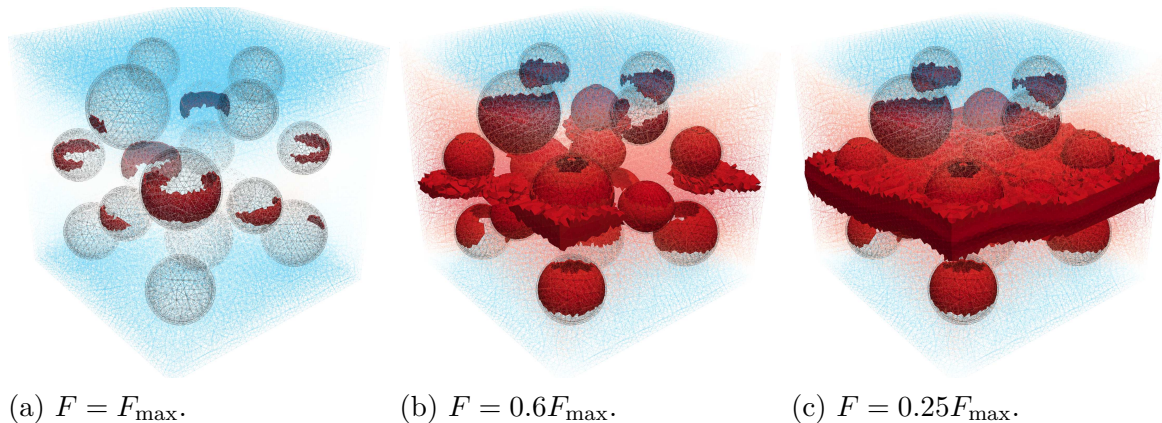(a) $F = F_{\max}$.　　　(b) $F = 0.6F_{\max}$.　　　(c) $F = 0.25F_{\max}$.

Figure 3.4: Damage plot of the adaptive backward Euler solution at different loading states after the post-peak. Elements with damage $\omega > 0.99$ are shown as solid elements, others as wireframe.

This issue can be solved by secant stiffness based methods. For each load step, the sequentially linear approach [Rots et al. 2008; Graça-e-Costa et al. 2012] repeatedly identifies critical elements and adapts their internal variables until equilibrium is reached. The method can be applied to smeared and discrete crack models and exhibits a "saw tooth" load-displacement relation.

3.3 Implicit-Explicit (IMPL-EX) method

An alternative is the implicit-explicit (IMPL-EX) scheme [Oliver et al. 2008]. It adapts the internal variables in all elements simultaneously once per load step to obtain the secant stiffness. This requires only minor changes to existing model implementations and smoothly approximates the load-displacement curve.

Even for nonlocal models that do not suffer from the instabilities of local models, IMPL-EX provides two benefits. First, the implementation of the method itself is less invasive and even the implementation of the mechanical models is simplified, because certain derivatives vanish. Secondly, it reduces the computational effort by improving the properties of the global matrix and by reducing the number of time steps required to finish the simulation. The latter is achieved by using error control schemes [Oliver et al. 2008; Blanco et al. 2007]. Each IMPL-EX iteration introduces an extrapolation error that depends on the time step length. The right choice of this time step ensures that the extrapolation error is limited to a prescribed value.

The IMPL-EX scheme and its application to the model are discussed next. Special focus is given to the development of a new class of adaptive time stepping schemes. The speedup of the method is then investigated for the mesoscale geometry shown above

Thomas Titscher

(Fig. 3.4).

3.3.1 Method

The implicit/explicit (IMPL-EX) scheme is a time integration scheme for nonlinear constitutive models. Their nonlinearities often arise from internal history variables α[2] of the model and their evolution equations. For a new time step $n + 1$, an extrapolated value $\tilde{\alpha}$ is used instead of evaluating the evolution equation. This extrapolation is the *explicit* stage of the algorithm and reads

$$\tilde{\alpha}_{n+1} = \alpha_n + \frac{\Delta t_{n+1}}{\Delta t_n}\left(\alpha_n - \alpha_{n-1}\right), \qquad (3.6)$$

where $\alpha_n = \alpha(t_n)$ and $\alpha_{n-1} = \alpha(t_{n-1})$ and the time step is defined as $\Delta t_n = t_n - t_{n-1}$. The modified system of equations is solved and this solution is used to determine α_{n+1} (without ˜) from the evolution equation. For the special case of a quasistatic isotropic damage model, this is also an explicit formula. For a general nonlinear model, this is not the case. Hence the name *implicit* stage.

This extrapolation has several implications:

- By extrapolating those variables based on previously calculated values, derivatives with respect the history variables vanish. In fact, they do not need to be implemented. Especially for derivatives of tensor invariants, this time-consuming and error-prone process can be avoided.

- In the case of the gradient-enhanced damage model, this also leads to a decoupling of the two differential equations. The two resulting systems of equations are solved separately. The numerical effort for solving a sparse system of equations scales worse than linear (often quadratically) with the number of degrees of freedom N. Thus, splitting the system is advantageous as $N^2 > 2(N/2)^2$.

- Each system of equations is now symmetric. This roughly halves the numerical cost.

- The extrapolation involves time steps that can be chosen freely. For smaller time steps, IMPL-EX converges to the backward Euler solution. A coarse time stepping, however, can give an approximation of the solution with a fraction of the numerical effort.

More details are presented in chapter *IMPL-EX Time Integration* of Paper 2.

---

[2]For the gradient-enhanced damage model, the strain-like history variable κ is used as the extrapolation variable. But for the general method, it refers to any internal variable, like a damage value in other formulations or a plastic strain.

3.3.2 Summary of adaptive IMPL-EX time stepping

The IMPL-EX scheme introduces an additional error, the extrapolation error of the internal variables. This error is influenced by the time step and smaller time steps will result in smaller extrapolation errors, but increase the overall computational cost. For softening models, the extrapolation error in the region of damage initiation is higher than in the elastic regime or towards a fully damaged state. To obtain a small overall error with a fixed time step, the small time steps required to resolve damage initiation have to be employed for the whole simulation. Additionally, this optimal value is hard to determine a priori.

Adaptive time stepping schemes address both problems. Their goal is to calculate the new time step such that it keeps the extrapolation error bounded. With the proper definition of the extrapolation error, this automatically results in smaller time steps in the region of damage initiation and larger ones elsewhere, which saves a significant number of iterations. Therefore, three main error categories are introduced in chapter *Adaptive IMPL-EX Time Stepping* of Paper 2 and are summarized here.

The absolute extrapolation error is the difference of the extrapolated value $\tilde{\alpha}$ after the explicit stage to the value α after the implicit stage. Applied to the gradient damage model with $\alpha = \kappa$ as the extrapolation variable, the point of damage initiation is not properly resolved. This is addressed by time stepping schemes based on the relative extrapolation error. They relate the absolute error to the previous value of the history variable. The time step is reduced around the damage initiation and increased towards full localization. This is quantified in a convergence analysis that relates the precision of the error control schemes with the computational effort. A third method is to directly limit damage growth to a fixed absolute value. This method excels at resolving the peak load, as this is the region where damage grows rapidly. In the post-peak region, however, the damage increments decrease exponentially. The comparison to a fixed absolute value is no longer a good indicator of the actual error.

3.3.3 Speedup of mesoscale simulations

The performance and precision of IMPL-EX is compared to a backward Euler integration for constant and adaptive time stepping in a double-notched tensile test (2D), a compression test of homogenized material (2D) and a mesoscale compression test (3D).

The latter one is already in the introductory part of this chapter and further discussed next. The geometry overview of Fig. 3.5a shows tetrahedron elements for the linear elastic aggregates and the nonlocal damage matrix. The CSDA interface is modeled with wedge (pentahedron) elements.

The resulting load-displacement curves for different time integration schemes are shown

Thomas Titscher
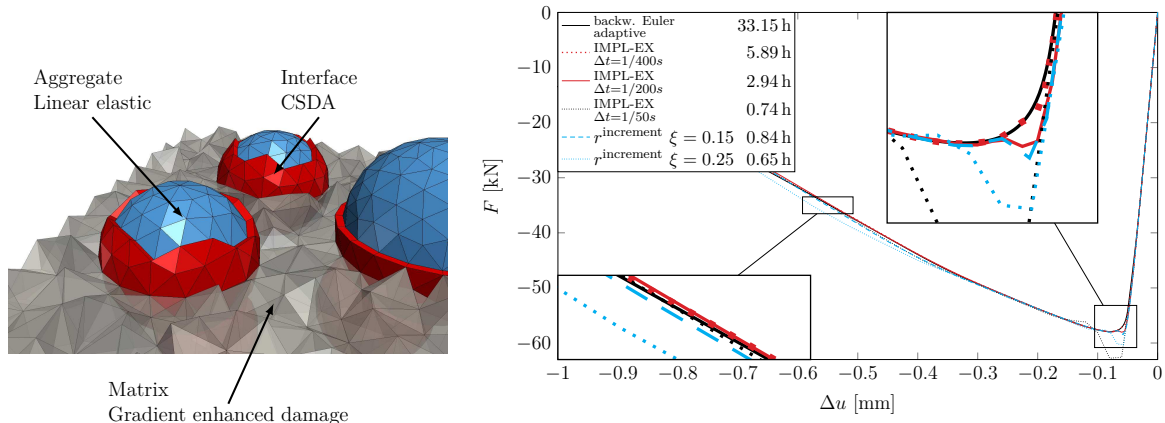
(a) Visualization of the mesoscale geometry and the material models.

(b) Load-displacement curves for different time integration schemes. The legend shows the solver time.

Figure 3.5: Setup and results of the mesoscale simulation of Fig. 3.4.

in Fig. 3.5b. There is almost no visible difference between the IMPL-EX solution with 400 fixed time steps and the adaptive backward Euler reference solution. With only 200 time steps, the solution suffers from a small oscillation near the peak load and continues very close to the equilibrium path. Compared with the backward Euler simulation, this results in a computational acceleration of ≈ 11 times. The adaptive scheme with $\xi = 0.15$ corresponds to 57 time steps and its accuracy is comparable to that of IMPL-EX with 200 fixed time steps. Thus, the acceleration compared with the adaptive backward Euler solution increases to ≈ 40 times. The reduced number of time steps is one factor for the reduced wall time. Another one is the numerical benefits of IMPL-EX mentioned in Section 3.3.1. The linear IMPL-EX system of equations requires a single solve compared to multiple iterations of the nonlinear backward Euler method. Additionally, the IMPL-EX system is symmetric and can be solved in a staggered, decoupled way which roughly halves the solution time of a single solve compared to the asymmetric coupled system of equations of the backward Euler method.

3.4 Time integration of a fatigue model

The development of numerical methods for reliable simulations of fatigue failure in structures and components has gained significant importance in the past decade. The main emphasis of the research is to reduce the computational costs required for realistic simulations of fatigue deterioration by means of continuum damage mechanics.

Formally, two time scales are introduced. The *micro*chronological scale describes the structural response arising from the high frequency load and corresponds to single load

cycles. Classically, the cycle is divided into a number of time steps. The computational cost is dominated by the solution of the governing nonlinear equations in each of those time steps. The damage growth over the full material life time is described on the *macro*chronological scale. The computational cost consists of repeated evaluations of the microchronological problem.

With about ten nonlinear solutions per cycle and possibly millions of cycles until material failure, it becomes clear that this straightforward cycle-by-cycle integration exceeds the computational resources. However, the damage accumulation on the microchronological scale is much smaller than the one on the macroscale. In this sense, fatigue is a multiscale phenomenon in time [Fish et al. 2002] and, analyzed as such, gives rise to several acceleration techniques on both scales.

Currently established methods to improve the computational efficiency of realistic simulations are cycle jump methods, asymptotic and almost periodic homogenization methods and Fourier transformation-based approaches that are further reviewed in [Chakraborty et al. 2013].

In asymptotic methods, the history variables and the response fields are approximated using an asymptotic expansion. The initial boundary value problem is then decomposed into averaged and oscillatory parts and dual-time scale algorithms are employed for its solution [Manchiraju et al. 2007]. Applications to fatigue failure for continuum mechanics is demonstrated in [Oskay et al. 2004; Fish et al. 2002; Fish et al. 2012].

The cycle jump methods first calculate the rate of damage (or any other history variable) of one cycle and use it then to extrapolate the evolution of the history variables for the subsequent cycles [Cojocaru et al. 2006; Kravchenko et al. 2014]. These omitted cycles are *jumped* over and explain the name of the method. A jump length of one cycle resembles the cycle-by-cycle integration. A larger jump length provides computational speedup, but introduces an extrapolation error.

As for the IMPL-EX scheme, the length of the jump is determined adaptively for optimal performance. In the very early and very late stage of the life time, the material behavior is dominated by large and varying damage scales and the time integration requires short jump lengths. In between, the material shows degradation with an almost constant damage rate and the size of the jumps can be noticeably increased while satisfying the prescribed extrapolation tolerance.

The Fourier transformation-based temporal integration (FTTI) combines two methods that address both the microchronological and the macrochronological scale separately [Kindrachuk et al. 2017]. The number of evaluated time steps on the microchronological scale is reduced by solving the problem in frequency space. And the adaptive cycle jump technique reduces the number of macrochronological time steps needed to reach material failure.

Thomas Titscher

3.4.1 Integration of the microchronological scale

Accumulation of damage during a single load cycle is usually negligible in a typical fatigue scenario. As a consequence, the damage state remains almost unchanged and the structural response follows the quasi periodic boundary conditions. It is therefore reasonable to assume that the unknown solution fields $\boldsymbol{u}$ can be approximated as Fourier series

$$\boldsymbol{u} := \boldsymbol{u}(\Upsilon, \tau) = \sum_{k \in \mathbb{Z}} \boldsymbol{u}_k(\Upsilon) e^{ik\omega\tau}. \tag{3.7}$$

In terms of the two time scales introduced above, $\Upsilon \in [0, N_f\ T]$ corresponds to the macrochronological problem and captures the loading cycles with period T until material failure after N_f cycles.

A time integration of the problem would discretize the microchronological scale $\tau \in [0, T]$ into N time steps and solve the governing equations for each of those. In this case, the governing equations are a gradient-enhanced damage model for fatigue. It consists of the momentum balance with the constitutive equation Eq. (2.4), where damage is driven by the nonlocal equivalent strains Eq. (3.3) and the fatigue evolution equations (2.8) and (2.9).

The presented Fourier approach first assumes a separation of scales, i.e. the evolution of the history variable within a cycle is small and does not influence the rate of change of the history variables within a cycle. This improves the condition of the resulting system of equations similarly to the explicit IMPL-EX stage. Instead of solving the system N times for every time step, it is solved k times to determine the unknown Fourier coefficients $\boldsymbol{u}_k$. For a sinusoidal load, this only requires to solve for the mean values $\boldsymbol{u}_0$ and the amplitudes $\boldsymbol{u}_1$. Then, according to Eq. (3.7), the solution fields can be cheaply evaluated at arbitrary time steps. This is used in a second step to approximate the damage growth of the cycle by integrating the local evolution equations (2.8) and (2.9) at the N time steps.

3.4.2 Adaptive cycle jump

In the region of an almost constant damage rate, the damage increment of a single cycle is extrapolated over many future cycles. Generally, this damage evolution on the macrochronological scale can be formulated as a first order ordinary differential equation. It relates the macrochronological change of damage to the microchronological damage increment of one loading cycle. The direct cycle jump method [Cojocaru et al. 2006] with its straightforward extrapolation is then a forward Euler discretization of this equation. It is, however, beneficial to employ second order methods like the midpoint rule applied by [Kindrachuk et al. 2017] or Heun's method used by [Peerlings et al. 2000]. They provide a significant advantage and are also used in this work.
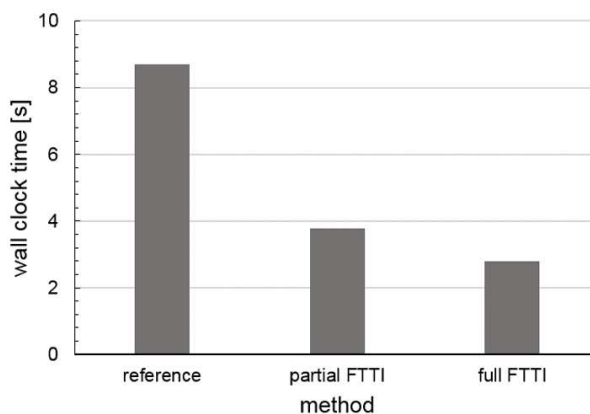
Figure 3.6: Averaged numerical efforts needed to integrate the microchronological cell (a single loading cycle), including finding the Fourier coefficients for the FTTI method.

The extrapolated damage after each jump introduces a deviation from the equilibrium state. This is caused by the solution fields that still correspond to the time step before the jump. Thus, they have to be updated while keeping the previously extrapolated history variables constant. This transforms the nonlinear asymmetric system of equations into two linear symmetric ones. The corresponding equations are shown in chapter 3.2 of Paper 3. They are very similar to the explicit IMPL-EX stage and result in the same performance benefits.

An adaptive jump length algorithm is introduced for the same reasons as the adaptive IMPL-EX time step. Here, the error measure is based on a relative error of the internal forces and the corresponding equations are shown in chapter 3.6 of Paper 3. The performance benefits of this method are discussed next.

3.4.3 FTTI for the gradient-enhanced damage model

The FTTI scheme refers to a combination of the Fourier-transformation based integration of the microchronological scale and the adaptive cycle jump on the macrochronological scale. But generally, both algorithms can be separated, e.g. by combining the adaptive cycle jump with any other integration technique of the microchronological problem. In chapter 4.3 of Paper 3, three such techniques are compared and the results are shown in Fig. 3.6.

In the case of the gradient-enhanced damage model, the Fourier approximation of Eq. (3.7) is first only applied to the displacement field. The nonlocal equivalent strain field is recovered by solving Eq. (3.3). This is referred to as the partial FTTI method and requires only half of the computational time of the reference full time integration. Applying Eq. (3.7) to both solution fields results in the full FTTI method and reduces the computational

time of integrating a single loading cycle to about a third of the reference.

The validational example of chapter 4.1 of Paper 3 is illustrated in Fig. 3.7 and shows the overall performance of the FTTI scheme. The two-dimensional void structure in Fig. 3.7a is uniaxially loaded with a triangular force that is approximated with five Fourier modes. The holes in the domain cause stress and strain concentrations which initiate damage on the hole boundaries. The damaged region expands until failure occurs.

The sensitivity analysis in Fig. 3.7b demonstrates the impact of the adaptive time stepping tolerance on the accuracy of the FTTI analysis. The solutions converge towards the reference cycle-by-cycle simulation as the tolerance *tol* decreases. For $tol = 0.02$, the FTTI solution and the direct numerical simulation are almost identical. Note that the adaptive time stepping properly recognizes the changing rates of material degradation and thus adequately adapts the macrochronological step size (jump). The jump length is gradually increased during the phase of almost constant damage growth and decreased when approaching failure.

The impact on the total solution time is shown in Fig. 3.7c, where the computational costs grows with increasing FTTI accuracy. For $tol = 0.02$ the full FTTI requires only 7.1% of the reference simulation time. This value further decreases to 4% for the higher tolerance value 0.04.
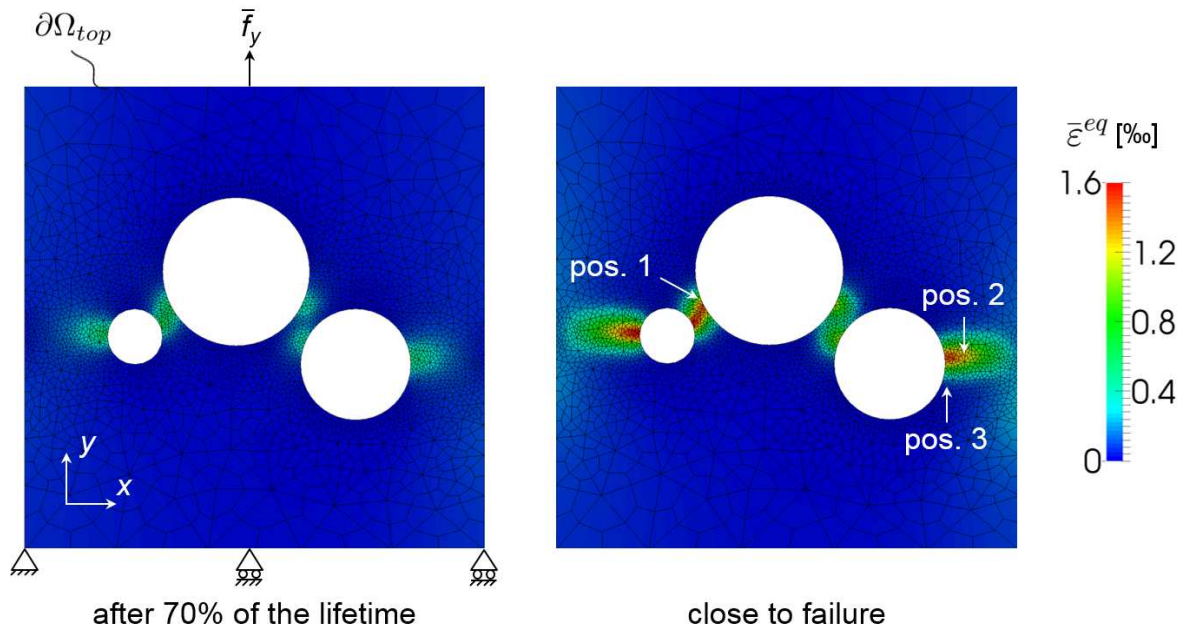
(a) Distribution of the nonlocal equivalent strain at two stages of the life time. The marked positions are chosen for the qualitative analysis.
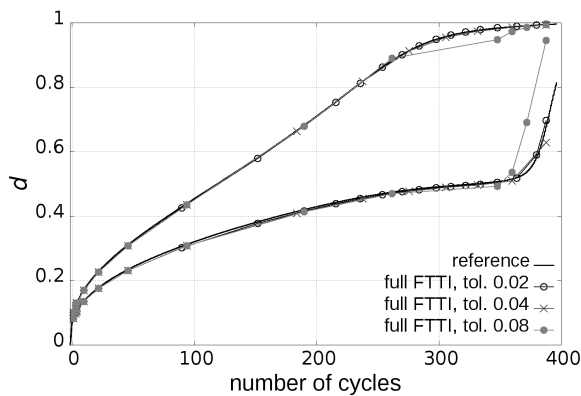
(b) Impact of the adaptive time stepping (ATS) algorithm for there values of the tolerance on the damage evolution. The upper lines represent pos. 2 and the lines below correspond to pos. 3.
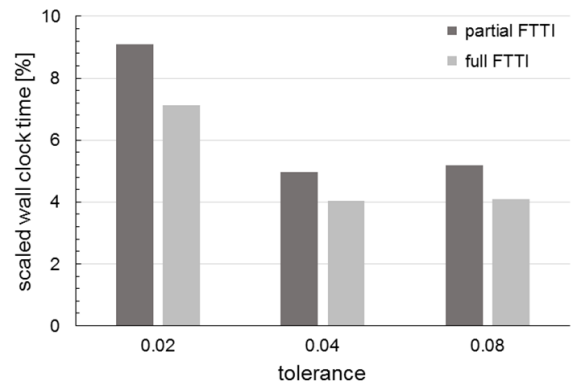
(c) Computational time required to perform fatigue simulations with the FTTI technique at various tolerances of the ATS.

Figure 3.7: Evaluation of the two-dimensional void structure under triangular cyclic loading.

4 Discussion

4.1 Conclusions

The complexity of the material makes numerical simulations of concrete a challenging task. From the various spatial scales that all influence the materials behavior, this work addresses the mesoscale that resolves the concrete aggregates. In contrast to simulations on finer scales, it makes numerical simulations up to lab specimen size feasible. And from the various physical processes, this work investigates the phenomenon of damage to model concrete fracture. This is done with regularized continuum damage models for quasistatic and fatigue failure as they allow integrating additional physical phenomena. In this thesis, three advancements were made towards more detailed mesoscale geometries and faster and more stable simulations on them.

Application of molecular dynamics simulations for the generation of dense concrete mesoscale geometries

The concrete mesoscale geometry is numerically represented by spherical particles. It is characterized by a particle size distribution that follows real concrete grading curves. Several sphere packing algorithm exist, to produce a non-overlapping packing of these particles in the virtual mesoscale specimen. Common sphere packing algorithms like the random sequential addition (RSA) algorithm excel at low particle volume fractions. Towards the high aggregate content of concrete, however, their efficiency drops until no valid packing is achieved. The previously placed and fixed particles block all the spots and finding a free random position becomes unlikely or impossible.

The employed event-driven molecular-dynamics (EDMD) algorithm allows particle rearrangements. This increases the volume fraction up to realistic values for concrete. The continuously growing particles move under free-flight dynamics and the simulation is advanced discretely to the next event, which is an elastic collision with either other particles or walls. Several optimization techniques are employed such that the numerical effort for the required collision predictions and the event organization only scales logarithmically with the number of particles. Depending on the specific grading curve used, the maximum volume fraction of the algorithm exceeds the RSA value by up to 11%.

The present EDMD algorithm with its growing particles excels at maximizing the distance Δd between particles. This is advantageous for finite element simulations as it increases the available space for meshing the matrix material between the aggregates. This is especially needed for nonlocal models that have to resolve a localized zone with several elements.

Implicit-Explicit Integration of Gradient-Enhanced Damage Models

One of such models is the implicit gradient-enhanced damage model by Peerlings et al. or Poh et al. that is employed in this work as the matrix material law in mesoscale simulations. Damage is driven by a nonlocal equivalent strain that serves as a localization limiter and prevents spurious mesh dependencies and strain localization.

The interfacial transition zone is modeled with thin elements and the continuous strong discontinuity approach (CSDA). It represents a discrete traction-separation law on the predefined crack paths around the aggregates within a continuum damage mechanics framework. In combination with the linear elastic aggregates, the quasistatic failure pattern of concrete is reproduced. The weaker ITZ material damages first, the aggregates start to debond and macroscopic cracks within the matrix material cause material failure.

Small snap-backs and bifurcation points in this complex geometry cause tiny time steps in a standard backward Euler solution algorithm. Thus, the implicit-explicit (IMPL-EX) method is introduced as an alternative. Its implementation is little invasive and mainly requires the extrapolation of the history variables. This decouples the system of equations and provides various numerical benefits. The backward Euler algorithm requires the full algorithmic stiffness, and the resulting monolithic system is nonlinear and asymmetric. The decoupling allows a subsequent solution of each subsystem, in which one tangent is linear and symmetric and the second tangent is constant. Additionally, off-diagonal terms in the algorithmic stiffness matrix are no longer required and only the block-diagonal matrix entries have to be computed/implemented.

There is a certain minimal time step for the backward Euler scheme which constrains the run time of the simulation. By accepting a loss in accuracy, the IMPL-EX scheme can find solutions with an arbitrary number of iterations. The actual acceleration, however, strongly depends on the problem. In a three-dimensional compression test, a reasonable approximation of an adaptive backward Euler solution is obtained with equidistant IMPL-EX time steps and an acceleration of ≈ 11 times. IMPL-EX extrapolation errors during the damage initiation have a larger influence than the same errors in an almost completely damaged material. Since smaller time steps lead to smaller errors, it is beneficial to concentrate the time steps around the point of damage initiation. This is achieved by using adaptive time stepping algorithms. The performance of three different classes of algorithms are assessed. The scheme that limits the relative error of the history variables performs best. It is capable of reducing the number of iterations while maintaining the

Thomas Titscher

accuracy. In the three-dimensional compression test mentioned previously, a significant acceleration ($\approx$ 40 times) is obtained.

A Fourier transformation-based method for gradient-enhanced modeling of fatigue

The computational costs of CDM fatigue simulations are usually not dominated by algorithmic instabilities, but simply by a high number of simulation time steps. This number is composed of the steps required to integrate a single loading cycle and the number of full cycles until material failure.

Basic fatigue behavior is introduced into the implicit gradient-enhanced damage model by modifying the evolution equation and damage is accumulated for each (positive) change of the nonlocal strains. Compared to empirical approaches like the Wöhler concept, this can resolve stress redistributions and order effects and, again, allows to include multiphysics phenomena.

The damage growth within one loading cycle corresponds to the microchronological scale and is small compared to the damage growth over the macrochronological scale of the materials life time. This scale separation allows to reduce the computational cost by two optimizations. The almost constant damage state within one cycle leads to a quasi-periodic structural response and the unknown solution fields can be approximated as Fourier series. Then, instead of solving the system of equations for each time step of the cycle, it is solved for a generally lower number of Fourier amplitudes.

The evolution of damage on the macrochronological scale is governed by the microchronological contribution by means of the adaptive cycle jump technique. The damage rates from single microchronological cycle evaluations are extrapolated over a high number of cycles using a second-order method. Each of those macrochronological steps is further accompanied by the determination of the global equilibrium.

Both techniques are combined to the Fourier transformation-based time integration (FTTI) scheme that accurately agrees with the reference fatigue response obtained through a direct numerical simulation of a load controlled test. Depending on the prescribed tolerance of the adaptive time stepping scheme, the FTTI technique predicted the fatigue loading history about 11 to 25 times faster than the reference simulation of the validation example.

4.2 Outlook on the future

This chapter contains some envisaged future developments on the topics of this thesis. The thesis presents a number of computational techniques that are devised to solve some of the numerical problems and performance issues arising in concrete mesoscale simulations. Thus, the models are chosen to show the basic phenomena of damage, but are not necessarily suited to completely represent real concrete material. This is especially true for the presented fatigue model. Without these techniques, however, the design of more sophisticated models is hard. They cannot be validated or calibrated, possibly due to instabilities, but certainly due to unmanageable computational costs. Thus, the optimization techniques can generally be seen as the basis for future model development.

In the context of fracture modeling, this includes a more accurate failure representation in compressive loading. For the fatigue model, a fatigue function that represents the damage evolution over the loading cycles of real concrete specimens has to be found. This should not be done by a curve fitting approach, but based on a physical understanding of the underlying processes. In a first step, the experimentally observable loading-unloading hysteresis has to be modeled by including (visco-)plasticity. It may then be necessary to additionally include slow-scale effects like creep and drying to account for the deformation caused by the mean load and the environmental conditions, respectively. For real concrete structures, the well-controlled experimental conditions are no longer present. Temperature and humidity changes that are eliminated in an experimental setup have to be included in the model. Depending on the application, the applied loads now have varying frequencies and amplitudes and can deviate from the uniaxial compression tested in experiments.

But there are also more specific research topics linked directly to the presented algorithms. The presented concrete mesoscale geometry is based on spherical aggregates, that work well with the EDMD algorithm, but are seldom found in real concrete. The collision time between two moving and growing spheres is predicted by solving a quadratic equation. An extension of the algorithm to ellipsoids has to also include angular velocities and is shown in [Ghossein et al. 2013]. Either this or the present algorithm can then be used to calculate a bounding sphere/ellipsoid distribution that fits arbitrary aggregate shapes as shown in Fig. 4.1.

The formation of macroscopic cracks in the later stages of both quasistatic and fatigue simulations require a proper resolution of the corresponding field variables. This is, however, not required in earlier stages where the fields are rather smooth and a coarser finite element resolution suffices. Thus, mesh adaptation and refinement strategies can further reduce the numerical costs of such simulations [Plaza et al. 2000]. A refinement step corresponds to an increased number of internal variables and requires adaptations to the IMPL-EX and FTTI algorithms. The extrapolation formulas shown in this work have to be enriched with further geometric information to allow the interpolation of the internal
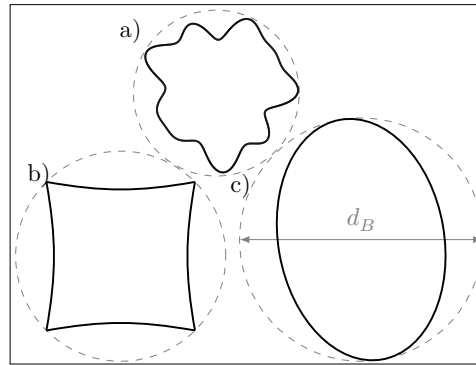
Thomas Titscher

Figure 4.1: The EDMD algorithm can be performed with bounding spheres of diameter d_B for each non-spherical particle. Arbitrary shapes e.g. a) based on spherical harmonics [Garboczi 2002], b) deformed cuboids or c) ellipsoids can be used.

variables from the current mesh to a possibly refined one before the extrapolation.

Bibliography

Alder, B. and T. Wainwright (1959). "Studies in Molecular Dynamics. 1. General Method". English. In: *Journal of chemical physics* 31.2, 459–466.

Allen, A. J., J. J. Thomas, and H. M. Jennings (2007). "Composition and density of nanoscale calcium–silicate–hydrate in cement". In: *Nature materials* 6.4, p. 311.

Ambati, M., T. Gerasimov, and L. De Lorenzis (2015). "A review on phase-field models of brittle fracture and a new fast hybrid formulation". In: *Computational Mechanics* 55.2, pp. 383–405.

Baranau, V. and U. Tallarek (2014). "Random-close packing limits for monodisperse and polydisperse hard spheres". In: *Soft Matter* 10.21, pp. 3826–3841.

Bažant, Z. P. and L. J. Najjar (1972). "Nonlinear water diffusion in nonsaturated concrete". In: *Matériaux et Construction* 5.1, pp. 3–20.

Bažant, Z. (Jan. 1976). "Instability, ductility, and size effect in strain-softening concrete". English (US). In: *Journal of Engineering Mechanics - ASCE* 102.2, pp. 331–344.

Bažant, Z. P. and M. Jirásek (2002). "Nonlocal Integral Formulations of Plasticity and Damage: Survey of Progress". In: *Journal of Engineering Mechanics* 128.11, pp. 1119–1149.

Bažant, Z. P. and R. L'Hermite (1988). *Mathematical modeling of creep and shrinkage of concrete*. Wiley New York.

Bažant, Z. P. and B. H. Oh (1985). "Microplane model for progressive fracture of concrete and rock". In: *Journal of Engineering Mechanics* 111.4, pp. 559–582.

Bažant, Z. P. and G. Pijaudier-Cabot (1989). "Measurement of characteristic length of nonlocal continuum". In: *Journal of Engineering Mechanics* 115.4, pp. 755–767.

Bažant, Z. P., M. R. Tabbara, M. T. Kazemi, and G. Pijaudier-Cabot (1990). "Random particle model for fracture of aggregate or fiber composites". In: *Journal of engineering mechanics* 116.8, pp. 1686–1705.

Bažant, Z. P. and K. Xu (1991). "Size effect in fatigue fracture of concrete". In: *ACI Materials Journal* 88.4, pp. 390–399.

Bažant, Z. (1985). "Mechanics of fracture and progressive cracking in concrete structures". In: *Fracture mechanics of concrete: Structural application and numerical calculation*. Springer, pp. 1–94.

Belytschko, T. and T. Black (1999). "Elastic crack growth in finite elements with minimal remeshing". In: *International journal for numerical methods in engineering* 45.5, pp. 601–620.

Blanco, S., J. Oliver, and A. Huespe (2007). "Contribuciones a la simulación numérica del fallo material en medios tridimensionales mediante la metodologia de discontinuidades fuertes de continuo". PhD thesis. Universitat Politécnica de Catalunya.

Breccolotti, M., M. F. Bonfigli, A. D'Alessandro, and A. L. Materazzi (2015). "Constitutive modeling of plain concrete subjected to cyclic uniaxial compressive loading". In: *Construction and Building materials* 94, pp. 172–180.

Bullard, J. W., H. M. Jennings, R. A. Livingston, A. Nonat, G. W. Scherer, J. S. Schweitzer, K. L. Scrivener, and J. J. Thomas (2011). "Mechanisms of cement hydration". In: *Cement and concrete research* 41.12, pp. 1208–1223.

Campbell, F. C. (2012). *Fatigue and fracture: understanding the basics*. ASM International.

Carol, I. and Z. P. Bazant (1997). "Damage and plasticity in microplane theory". In: *International Journal of Solids and Structures* 34.29, pp. 3807–3835.

Carol, I., C. M. López, and O. Roa (2001). "Micromechanical analysis of quasi-brittle materials using fracture-based interface elements". In: *International Journal for Numerical Methods in Engineering* 52.1-2, pp. 193–215.

Chakraborty, P. and S. Ghosh (2013). "Accelerating cyclic plasticity simulations using an adaptive wavelet transformation based multitime scaling method". In: *International Journal for Numerical Methods in Engineering* 93.13, pp. 1425–1454.

Cojocaru, D. and A. M. Karlsson (2006). "A simple numerical method of cycle jumps for cyclically loaded structures". In: *International Journal of fatigue* 28.12, pp. 1677–1689.

Comi, C. and U. Perego (2001). "Fracture energy based bi-dissipative damage model for concrete". In: *International journal of solids and structures* 38.36-37, pp. 6427–6454.

Cosserat, E. and F. Cosserat (1909). "Théorie des corps déformables". In:

Cundall, P. A. and O. D. Strack (1979). "A discrete numerical model for granular assemblies". In: *geotechnique* 29.1, pp. 47–65.

Cusatis, G., D. Pelessone, and A. Mencarelli (2011). "Lattice discrete particle model (LDPM) for failure behavior of concrete. I: Theory". In: *Cement and Concrete Composites* 33.9, pp. 881–890.

Dias, I., J. Oliver, and O. Lloberas-Valls (2018). "Strain-injection and crack-path field techniques for 3D crack-propagation modelling in quasi-brittle materials". In: *International Journal of Fracture* 212.1, pp. 67–87.

DIN 1045 (Aug. 2008). *Concrete, reinforced and prestressed concrete structures - Part 2: Concrete - Specification, performance, production and conformity - Application rules for DIN EN 206*. Norm.

Drucker, D. C. and W. Prager (1952). "Soil mechanics and plastic analysis or limit design". In: *Quarterly of applied mathematics* 10.2, pp. 157–165.

Erdogan, F. and G. Sih (1963). "On the crack extension in plates under plane loading and transverse shear". In: *Journal of basic engineering* 85.4, pp. 519–525.

Faria, R., J. Oliver, and M. Cervera (1998). "A strain-based plastic viscous-damage model for massive concrete structures". In: *International journal of solids and structures* 35.14, pp. 1533–1558.

Feenstra, P. H. and R. De Borst (1996). "A composite plasticity model for concrete". In: *International Journal of Solids and Structures* 33.5, pp. 707–730.

Fish, J., M. Bailakanavar, L. Powers, and T. Cook (2012). "Multiscale fatigue life prediction model for heterogeneous materials". In: *International Journal for Numerical Methods in Engineering* 91.10, pp. 1087–1104.

Thomas Titscher

Fish, J. and Q. Yu (2002). "Computational mechanics of fatigue and life predictions for composite materials and structures". In: *Computer methods in applied mechanics and engineering* 191.43, pp. 4827–4849.

Garboczi, E. J. (2002). "Three-dimensional mathematical analysis of particle shape using X-ray tomography and spherical harmonics: Application to aggregates used in concrete". In: *Cement and concrete research* 32.10, pp. 1621–1638.

Gawin, D., F. Pesavento, and B. Schrefler (2007). "Modelling creep and shrinkage of concrete by means of effective stresses". In: *Materials and Structures* 40.6, pp. 579–591.

Gawin, D., F. Pesavento, and B. A. Schrefler (2011). "What physical phenomena can be neglected when modelling concrete at high temperature? A comparative study. Part 1: Physical phenomena and mathematical model". In: *International journal of solids and structures* 48.13, pp. 1927–1944.

Geers, M. (1999a). "Enhanced solution control for physically and geometrically nonlinear problems. Part I—the subplane control approach". In: *International Journal for Numerical Methods in Engineering* 46.2, pp. 177–204.

Geers, M. (1999b). "Enhanced solution control for physically and geometrically nonlinear problems. Part II—comparative performance analysis". In: *International Journal for Numerical Methods in Engineering* 46.2, pp. 205–230.

Geers, M., R. De Borst, and W. Brekelmans (1996). "Computing strain fields from discrete displacement fields in 2D-solids". In: *International Journal of Solids and Structures* 33.29, pp. 4293–4307.

Ghossein, E. and M. Lévesque (2013). "Random generation of periodic hard ellipsoids based on molecular dynamics: A computationally-efficient algorithm". In: *Journal of Computational Physics* 253, pp. 471–490.

Graça-e-Costa, R., J. Alfaiate, D. Dias-da-Costa, and L. J. Sluys (Nov. 2012). "A non-iterative approach for the modelling of quasi-brittle materials". In: *International Journal of Fracture* 178.1, pp. 281–298.

Grassl, P. and M. Jirásek (2006). "Damage-plastic model for concrete failure". In: *International journal of solids and structures* 43.22-23, pp. 7166–7196.

Grassl, P. and R. Rempling (2008). "A damage-plasticity interface approach to the meso-scale modelling of concrete subjected to cyclic compressive loading". In: *Engineering Fracture Mechanics* 75.16, pp. 4804–4818.

Griffith, A. A. (1921). "VI. The phenomena of rupture and flow in solids". In: *Philosophical transactions of the royal society of london. Series A, containing papers of a mathematical or physical character* 221.582-593, pp. 163–198.

Häfner, S., S. Eckardt, T. Luther, and C. Könke (2006). "Mesoscale modeling of concrete: Geometry and numerics". In: *Computers & structures* 84.7, pp. 450–461.

Hales, T. C. (2005). "A proof of the Kepler conjecture". In: *Annals of mathematics*, pp. 1065–1185.

Hill, R. (1958). "A general theory of uniqueness and stability in elastic-plastic solids". In: *Journal of the Mechanics and Physics of Solids* 6.3, pp. 236–249.

Hillerborg, A., M. Modéer, and P.-E. Petersson (1976). "Analysis of crack formation and crack growth in concrete by means of fracture mechanics and finite elements". In: *Cement and concrete research* 6.6, pp. 773–781.

Hlobil, M., V. Šmilauer, and G. Chanvillard (2016). "Micromechanical multiscale fracture model for compressive strength of blended cement pastes". In: *Cement and Concrete Research* 83, pp. 188–202.

Hughes, T. J. (2012). *The finite element method: linear static and dynamic finite element analysis.* Courier Corporation.

Hüsken, G. and H. Brouwers (2008). "A new mix design concept for earth-moist concrete: A theoretical and experimental study". In: *Cement and Concrete Research* 38.10, pp. 1246–1259.

Jirásek, M. and B. Patzák (2002a). "Consistent tangent stiffness for nonlocal damage models". In: *Computers & structures* 80.14-15, pp. 1279–1293.

Jirásek, M. (1998). "Nonlocal models for damage and fracture: comparison of approaches". In: *International Journal of Solids and Structures* 35.31-32, pp. 4133–4145.

Jirásek, M. (2007). "Mathematical analysis of strain localization". In: *Revue européenne de génie civil* 11.7-8, pp. 977–991.

Jirásek, M. and M. Bauer (2012). "Numerical aspects of the crack band approach". In: *Computers & Structures* 110, pp. 60–78.

Jirásek, M. and Z. P. Bažant (2002b). *Inelastic analysis of structures.* John Wiley & Sons.

Johannesson, B. and U. Nyman (2010). "A numerical approach for non-linear moisture flow in porous materials with account to sorption hysteresis". In: *Transport in porous media* 84.3, pp. 735–754.

Kachanov, L. (2013). *Introduction to continuum damage mechanics.* Vol. 10. Springer Science & Business Media.

Kachanov, L. (1958). "Rupture time under creep conditions". In: *Izv. Akad. Nauk SSSR* 8, pp. 26–31.

Kansal, A. R., S. Torquato, and F. H. Stillinger (2002a). "Computer generation of dense polydisperse sphere packings". In: *The Journal of Chemical Physics* 117.18, pp. 8212–8218.

Kansal, A. R., S. Torquato, and F. H. Stillinger (2002b). "Diversity of order and densities in jammed hard-particle packings". In: *Physical Review E* 66.4, p. 041109.

Kim, J.-K. and Y.-Y. Kim (1996). "Experimental study of the fatigue behavior of high strength concrete". In: *Cement and Concrete Research* 26.10, pp. 1513–1523.

Kindrachuk, V. M., M. Thiele, and J. F. Unger (2015). "Constitutive modeling of creep-fatigue interaction for normal strength concrete under compression". In: *International Journal of Fatigue* 78, pp. 81–94.

Kindrachuk, V. M., T. Titscher, and J. F. Unger (2018). "A Fourier transformation-based method for gradient-enhanced modeling of fatigue". In: *International Journal for Numerical Methods in Engineering* 114.2, pp. 196–214.

Kindrachuk, V. M. and J. F. Unger (2017). "A Fourier transformation-based temporal integration scheme for viscoplastic solids subjected to fatigue deterioration". In: *International Journal of Fatigue* 100, pp. 215–228.

Thomas Titscher

Kravchenko, G., B. Karunamurthy, and H. E. Pettermann (2014). "FEM Study of Fatigue Crack Growth in a Power Semiconductor Chip Subjected to Transient Thermal Loading". In: *Procedia Materials Science* 3. 20th European Conference on Fracture, pp. 63–70.

Kuna, M. and S. Roth (2015). "General remarks on cyclic cohesive zone models". In: *International Journal of Fracture* 196.1-2, pp. 147–167.

Kupfer, H., H. K. Hilsdorf, and H. Rusch (1969). "Behavior of concrete under biaxial stresses". In: *Journal Proceedings*. Vol. 66. 8, pp. 656–666.

Ladeveze, P. and J. Lemaitre (1984). "Damage effective stress in quasi unilateral conditions". In: *16th International congress of theoretical and applied mechanics, Lyngby, Denmark.*

Loehnert, S., D. Mueller-Hoeppe, and P. Wriggers (2011). "3D corrected XFEM approach and extension to finite deformation theory". In: *International Journal for Numerical Methods in Engineering* 86.4-5, pp. 431–452.

Lubachevsky, B. D. and F. H. Stillinger (1990). "Geometric properties of random disk packings". English. In: *Journal of Statistical Physics* 60.5-6, pp. 561–583.

Lubliner, J. (2008). *Plasticity theory.* Courier Corporation.

Lundgren, K. and K. Gylltoft (2000). "A model for the bond between concrete and reinforcement". In: *Magazine of Concrete Research* 52.1, pp. 53–63.

Mahal, M., T. Blanksvärd, B. Täljsten, and G. Sas (2015). "Using digital image correlation to evaluate fatigue behavior of strengthened reinforced concrete beams". In: *Engineering Structures* 105, pp. 277–288.

Manchiraju, S., M. Asai, and S. Ghosh (2007). "A dual-time-scale finite element model for simulating cyclic deformation of polycrystalline alloys". In: *The Journal of Strain Analysis for Engineering Design* 42.4, pp. 183–200.

Marigo, J. (1985). "Modelling of brittle and fatigue damage for elastic material by growth of microvoids". In: *Engineering Fracture Mechanics* 21.4, pp. 861–874.

May, S., J. Vignollet, and R. de Borst (2016). "A new arc-length control method based on the rates of the internal and the dissipated energy". In: *Engineering Computations* 33.1, pp. 100–115.

Mazars, J. (1986). "A description of micro-and macroscale damage of concrete structures". In: *Engineering Fracture Mechanics* 25.5-6, pp. 729–737.

Mazars, J. and G. Pijaudier-Cabot (1989). "Continuum damage theory – application to concrete". In: *Journal of Engineering Mechanics* 115.2, pp. 345–365.

Medeiros, A., X. Zhang, G. Ruiz, C. Y. Rena, and M. d. S. L. Velasco (2015). "Effect of the loading frequency on the compressive fatigue behavior of plain and fiber reinforced concrete". In: *International Journal of Fatigue* 70, pp. 342–350.

Menetrey, P. and K. Willam (1995). "Triaxial failure criterion for concrete and its generalization". In: *Structural Journal* 92.3, pp. 311–318.

Miehe, C., F. Welschinger, and M. Hofacker (2010). "Thermodynamically consistent phase-field models of fracture: Variational principles and multi-field FE implementations". In: *International Journal for Numerical Methods in Engineering* 83.10, pp. 1273–1311.

Mindess, S., J. Young, and D. Darwin (2003). *Concrete.* Prentice Hall.

Mises, R. v. (1913). "Mechanik der festen Körper im plastisch-deformablen Zustand". In: *Nachrichten von der Gesellschaft der Wissenschaften zu Göttingen, Mathematisch-Physikalische Klasse* 1913, pp. 582–592.

Moës, N. and T. Belytschko (2002). "Extended finite element method for cohesive crack growth". In: *Engineering fracture mechanics* 69.7, pp. 813–833.

Moës, N., J. Dolbow, and T. Belytschko (1999). "A finite element method for crack growth without remeshing". In: *International journal for numerical methods in engineering* 46.1, pp. 131–150.

Murdock, J. W. (1965). *A critical review of research on fatigue of plain concrete.* Tech. rep. University of Illinois at Urbana Champaign, College of Engineering …

Nagai, G. and T. Yamada (2006). "Three-Dimensional Finite Element Modeling for Concrete Materials Using Digital Image and Embedded Discontinuous Element". In: *International Journal for Multiscale Computational Engineering* 4.4, pp. 461–474.

Needleman, A. (1988). "Material rate dependence and mesh sensitivity in localization problems". In: *Computer methods in applied mechanics and engineering* 67.1, pp. 69–85.

Nguyen, T., J. Yvonnet, Q.-Z. Zhu, M. Bornert, and C. Chateau (2015). "A phase field method to simulate crack nucleation and propagation in strongly heterogeneous materials from direct imaging of their microstructure". In: *Engineering Fracture Mechanics* 139, pp. 18–39.

Noorsuhada, M. (2016). "An overview on fatigue damage assessment of reinforced concrete structures with the aid of acoustic emission technique". In: *Construction and Building Materials* 112, pp. 424–439.

Oliver, J. (1989). "A consistent characteristic length for smeared cracking models". In: *International Journal for Numerical Methods in Engineering* 28.2, pp. 461–474.

Oliver, J., A. Huespe, S. Blanco, and D. Linero (2006). "Stability and robustness issues in numerical modeling of material failure with the strong discontinuity approach". In: *Computer Methods in Applied Mechanics and Engineering* 195.52, pp. 7093–7114.

Oliver, J., A. Huespe, and J. Cante (2008). "An implicit/explicit integration scheme to increase computability of non-linear material and contact/friction problems". In: *Computer Methods in Applied Mechanics and Engineering* 197.21, pp. 1865–1889.

Oliver, J., A. Huespe, M. Pulido, and E. Chaves (2002). "From continuum mechanics to fracture mechanics: the strong discontinuity approach". In: *Engineering Fracture Mechanics* 69.2, pp. 113–136.

Oliver, J., M. Cervera, S. Oller, and J. Lubliner (1990). "Isotropic damage models and smeared crack analysis of concrete". In: *Proc. SCI-C Computer Aided Analysis and Design of Concrete Structures.* Vol. 945958.

Ollivier, J., J. Maso, and B. Bourdette (1995). "Interfacial transition zone in concrete". In: *Advanced cement based materials* 2.1, pp. 30–38.

Oskay, C. and J. Fish (2004). "Fatigue life prediction using 2-scale temporal asymptotic homogenization". In: *International Journal for Numerical Methods in Engineering* 61.3, pp. 329–359.

Ottosen, N. S. (1977). "A failure criterion for concrete". In: *American Society of Civil Engineers. Engineering Mechanics Division. Journal* 103.4, pp. 527–535.

Thomas Titscher

Paul, B., M. Ndeffo, P. Massin, and N. Moës (2017). "An integration technique for 3D curved cracks and branched discontinuities within the extended finite element method". In: *Finite Elements in Analysis and Design* 123, pp. 19–50.

Peerlings, R., R. de Borst, W. Brekelmans, and M. Geers (2002). "Localisation issues in local and nonlocal continuum approaches to fracture". In: *European Journal of Mechanics - A/Solids* 21.2, pp. 175–189.

Peerlings, R. H., R. de Borst, W. M. Brekelmans, and J. De Vree (1996). "Gradient enhanced damage for quasi-brittle materials". In: *International Journal for numerical methods in engineering* 39.19, pp. 3391–3403.

Peerlings, R. H., W. M. Brekelmans, R. de Borst, and M. G. Geers (2000). "Gradient-enhanced damage modelling of high-cycle fatigue". In: *International Journal for Numerical Methods in Engineering* 49.12, pp. 1547–1569.

Pietruszczak, S. and Z. Mroz (1981). "Finite element analysis of deformation of strain-softening materials". In: *International Journal for Numerical Methods in Engineering* 17.3, pp. 327–334.

Pijaudier–Cabot, G. and Z. P. Bažant (1987). "Nonlocal Damage Theory". In: *Journal of Engineering Mechanics* 113.10, pp. 1512–1533.

Plaza, A. and G. Carey (2000). "Local refinement of simplicial grids based on the skeleton". In: *Applied Numerical Mathematics* 32.2, pp. 195–218.

Poh, L. H. and G. Sun (2017). "Localizing gradient damage model with decreasing interactions". In: *International Journal for Numerical Methods in Engineering* 110.6, pp. 503–522.

Pramono, E. and K. Willam (1989). "Fracture energy-based plasticity formulation of plain concrete". In: *Journal of Engineering Mechanics* 115.6, pp. 1183–1204.

Raithby, K. (1979). "Flexural fatigue behaviour of plain concrete". In: *Fatigue of Engineering Materials and Structures* 2.

Riks, E. (1979). "An incremental approach to the solution of snapping and buckling problems". In: *International journal of solids and structures* 15.7, pp. 529–551.

Rots, J. G., B. Belletti, and S. Invernizzi (2008). "Robust modeling of RC structures with an "event-by-event" strategy". In: *Engineering Fracture Mechanics* 75.3. International Conference of Crack Paths, pp. 590–614.

Saroukhani, S., R. Vafadari, and A. Simone (2012). "A simplified implementation of a gradient-enhanced damage model with transient length scale effects". In: *Computational Mechanics* 51.6, pp. 899–909.

Schlangen, E. and J. G. M. Van Mier (1992). "Simple lattice model for numerical simulation of fracture of concrete materials and structures". In: *Materials and Structures* 25.9, pp. 534–542.

Sidoroff, F. (1981). "Description of anisotropic damage application to elasticity". In: *Physical Non-Linearities in Structural Analysis*. Springer, pp. 237–244.

Sima, J. F., P. Roca, and C. Molins (2008). "Cyclic constitutive model for concrete". In: *Engineering structures* 30.3, pp. 695–706.

Simo, J. C. and T. J. Hughes (2006). *Computational inelasticity*. Vol. 7. Springer Science & Business Media.

Simo, J. C. and J. Ju (1987). "Strain-and stress-based continuum damage models—I. Formulation". In: *International journal of solids and structures* 23.7, pp. 821–840.

Simo, J. C., J. Oliver, and F. Armero (1993). "An analysis of strong discontinuities induced by strain-softening in rate-independent inelastic solids". In: *Computational mechanics* 12.5, pp. 277–296.

Simone, A., H. Askes, R. Peerlings, and L. Sluys (2003). "Interpolation requirements for implicit gradient-enhanced continuum damage models". In: *International Journal for Numerical Methods in Biomedical Engineering* 19.7, pp. 563–572.

Simone, A., H. Askes, and L. J. Sluys (2004). "Incorrect initiation and propagation of failure in non-local and gradient-enhanced media". In: *International Journal of Solids and Structures* 41.2, pp. 351–363.

Sinaie, S., A. Heidarpour, X. Zhao, and J. Sanjayan (2015). "Effect of size on the response of cylindrical concrete samples under cyclic loading". In: *Construction and Building Materials* 84, pp. 399–408.

Skoge, M., A. Donev, F. H. Stillinger, and S. Torquato (Oct. 2006). "Packing hyperspheres in high-dimensional Euclidean spaces". In: *Physical Review E* 74 (4), p. 041127.

Sluys, L. and R. De Borst (1992). "Wave propagation and localization in a rate-dependent cracked medium—model formulation and one-dimensional examples". In: *International Journal of Solids and Structures* 29.23, pp. 2945–2958.

Thiele, M. (2015). "Experimentelle Untersuchung und Analyse der Schädigungsevolution in Beton unter hochzyklischen Ermüdungsbeanspruchungen". PhD thesis. Technical University Berlin.

Titscher, T., J. Oliver, and J. F. Unger (2019). "Implicit–Explicit Integration of Gradient-Enhanced Damage Models". In: *Journal of Engineering Mechanics* 145.7, p. 04019040.

Titscher, T. and J. F. Unger (2015). "Application of molecular dynamics simulations for the generation of dense concrete mesoscale geometries". In: *Computers & Structures* 158, pp. 274–284.

Top 500 (2019). *Top 500 June 2019*. `https://www.top500.org/lists/2019/06/`. Accessed: 2019-06-15.

Torquato, S. and F. H. Stillinger (Sept. 2010). "Jammed hard-particle packings: From Kepler to Bernal and beyond". In: *Reviews of Modern Physics* 82 (3), pp. 2633–2672.

Toselli, A. and O. Widlund (2006). *Domain decomposition methods-algorithms and theory*. Vol. 34. Springer Science & Business Media.

Truesdell, C. (1952). "The mechanical foundations of elasticity and fluid dynamics". In: *Journal of Rational Mechanics and Analysis* 1, pp. 125–300.

Unger, J. and S. Eckardt (2011a). "Multiscale modeling of concrete". In: *Archives of Computational Methods in Engineering* 18.3, p. 341.

Unger, J. F. (2009). "Neural networks in a multiscale approach for concrete". PhD thesis.

Unger, J. F., S. Eckardt, and C. Könke (2007). "Modelling of cohesive crack growth in concrete structures with the extended finite element method". In: *Computer methods in applied mechanics and engineering* 196.41-44, pp. 4087–4100.

Unger, J. F., S. Eckardt, and C. Könke (2011b). "A mesoscale model for concrete to simulate mechanical failure". In: *Computers and Concrete* 8.4, pp. 401–423.

Verhoosel, C. V., J. J. Remmers, and M. A. Gutiérrez (2009). "A dissipation-based arclength method for robust simulation of brittle and ductile failure". In: *International Journal for Numerical Methods in Engineering* 77.9, pp. 1290–1321.

Vree, J. de, W. Brekelmans, and M. van Gils (1995). "Comparison of nonlocal approaches in continuum damage mechanics". In: *Computers & Structures* 55.4, pp. 581–588.

Wang, Z. M., A. K. H. Kwan, and H. C. Chan (1999). "Mesoscopic study of concrete I: generation of random aggregate structure and finite element mesh ". In: *Computers & Structures* 70.5, pp. 533–544.

Widom, B. (1966). "Random Sequential Addition of Hard Spheres to a Volume". In: *The Journal of Chemical Physics* 44.10, pp. 3888–3894.

Willebeek-LeMair, M. H. and A. P. Reeves (1993). "Strategies for dynamic load balancing on highly parallel computers". In: *IEEE Transactions on parallel and distributed systems* 4.9, pp. 979–993.

Wriggers, P. and S. O. Moftah (2006). "Mesoscale models for concrete: Homogenisation and damage behaviour". In: *Finite Elements in Analysis and Design* 42.7, pp. 623–636.

Zubelewicz, A. and Z. P. Bažant (1987). "Interface element modeling of fracture in aggregate composites". In: *Journal of engineering mechanics* 113.11, pp. 1619–1630.

[Appendix]

https://doi.org/10.1016/j.compstruc.2015.06.008
https://www.sciencedirect.com/science/article/abs/pii/S0045794915001972

https://doi.org/10.1061/ (ASCE)EM.1943-7889.0001608.
https://ascelibrary.org/doi/abs/10.1061/%28ASCE%29EM.1943-7889.0001608

https://doi.org/10.1002/nme.5740
https://onlinelibrary.wiley.com/doi/abs/10.1002/nme.5740

Thomas Titscher